

# Mutual Information Regularization for Weakly-supervised RGB-D Salient Object Detection

Aixuan Li, Yuxin Mao, Jing Zhang, Yuchao Dai\*

**Abstract**—In this paper, we present a weakly-supervised RGB-D salient object detection model via scribble supervision. Specifically, as a multimodal learning task, we focus on effective multimodal representation learning via inter-modal mutual information regularization. In particular, following the principle of disentangled representation learning, we introduce a mutual information upper bound with a mutual information minimization regularizer to encourage the disentangled representation of each modality for salient object detection. Based on our multimodal representation learning framework, we introduce an asymmetric feature extractor for our multimodal data, which is proven more effective than the conventional symmetric backbone setting. We also introduce multimodal variational auto-encoder as stochastic prediction refinement techniques, which takes pseudo labels from the first training stage as supervision and generates refined prediction. Experimental results on benchmark RGB-D salient object detection datasets verify both effectiveness of our explicit multimodal disentangled representation learning method and the stochastic prediction refinement strategy, achieving comparable performance with the state-of-the-art fully supervised models. Our code and data are available at: <https://github.com/baneitxiaomai/MIRV>.

**Index Terms**—Weakly-supervised, Salient Object Detection, Mutual Information Regularization

## I. INTRODUCTION

THE advance of existing saliency detection techniques relies greatly on the large-scale pixel-wise labeled training datasets, *e.g.* DUTS [1] and MSRA10K dataset [2] for RGB saliency detection, and NJU2K [3], NLPR [4] and COME dataset [5] for RGB-D saliency detection, where the labeling is usually time-consuming and expensive. Alternatively, saliency detection models can be trained in a weakly-supervised manner, where the weak labels can be image-level labels [6]–[11], scribble supervisions [12]–[14], bounding boxes [15] and *etc.* Considering both labeling efficiency and depth’s contribution as structure-preserving guidance, we work on scribble-supervised RGB-D salient object detection.

Our method includes three cascaded steps (see Fig. 1): 1) initial prediction estimation; 2) progressive prediction refinement with mutual information minimization [16], [17] as a regularizer; 3) second stage prediction refinement via multimodal variational auto-encoder [18]–[20]. For the estimation process, following the conventional dense prediction

models, we adopt backbone models, *i.e.* VGG16 or ResNet50, with a decoder to generate the initial prediction. Within the progressive refinement process, we first employ the tree-energy loss [21], a minimum spanning tree based online prediction refinement technique, to get the structure refined prediction. Then, to extensively explore the contribution of multimodal data for our weakly-supervised learning task, we present inter-modal mutual information minimization via mutual information regularization [16], achieving disentangled representation learning [22] to extensively explore the contribution of each modality for RGB-D saliency detection.

Different from existing RGB-D saliency detection models [5], [14], [23] that use symmetric feature extractors for both modalities, we observe the encoding abilities of different backbones differ in generating reliable feature representation of the dense segmentation task (see Fig. 2). Based on this, we introduce asymmetric feature extractors, where different backbones are used for RGB image and depth data.

Further, unlike existing approaches that focus on enhancing the fusion of features from different modalities via attention modules [24]–[28], we explore the use of mutual information estimation to explicitly explore the contribution of depth for weakly-supervised RGB-D saliency detection. Specifically, we apply a tighter upper bound [16] of cross-modal mutual information estimation compared with [5] following disentangled representation learning, achieving more reliable cross-modal complementary information exploration.

Also, our stochastic prediction refinement technique via multimodal variational auto-encoder [18]–[20] is proven more effective in generating robust and refined predictions to reduce the error propagation compared with existing pseudo labeling techniques or the post-hoc refinement methods (see Table V), *i.e.* denseCRF [29].

We summarize our main contributions as:

- 1) We introduce a mutual information optimization method to explicitly model the contribution of RGB and depth for weakly-supervised RGB-D saliency detection;
- 2) We present asymmetric feature extractors, taking advantage of different backbones’ encoding abilities to achieve more reliable feature representation;
- 3) We present a multimodal variational auto-encoder framework as the second stage refinement solution to refine model prediction, which is proven more robust to error propagation issues caused by pseudo labeling.

## II. RELATED WORK

**RGB-D Saliency Detection:** As a multimodal learning task, most of the existing RGB-D saliency detection models [4],

Aixuan Li, Yuxin Mao and Yuchao Dai are with School of Electronics and Information, Northwestern Polytechnical University, Xi’an, China and State Key Laboratory of Integrated Services Networks (Xidian University).

Jing Zhang is with School of Computing, the Australian National University, Canberra, Australia (zjnwpu@gmail.com).

Yuchao Dai is the corresponding author (daiyuchao@nwpu.edu.cn). This work was supported in part by the National Natural Science Foundation of China (No. 62271410).

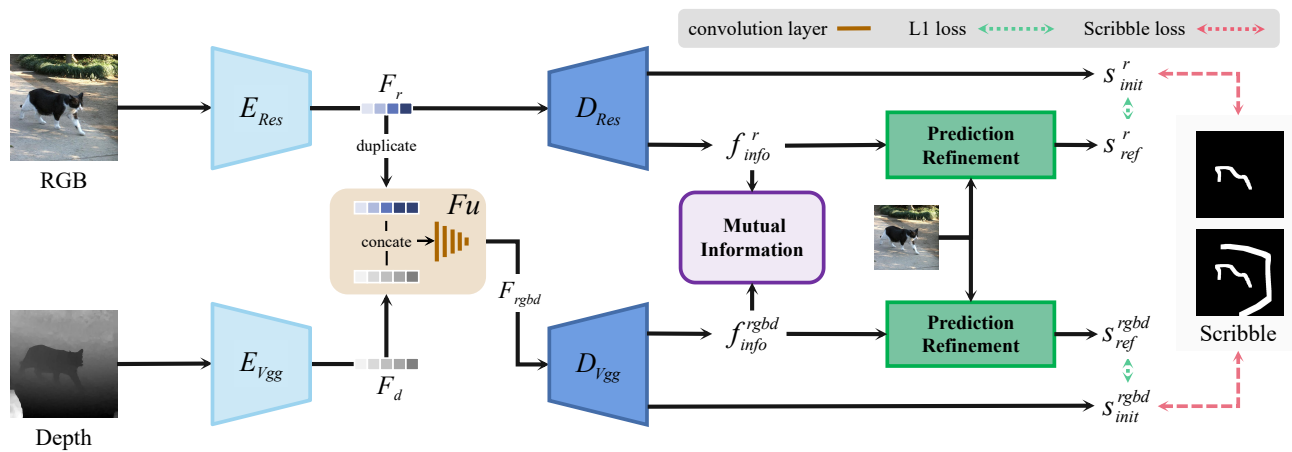


Fig. 1. Overview of the proposed framework. We propose *Asymmetric Encoders* to provide task-specific features ( $F_r$  and  $F_d$ ) for RGB and depth image. After cross-level fusion ( $F_u$ ), we utilize *Mutual Information* as a regularization term to emphasize the information specificity of the different modalities. And to optimize the dense predictions, we add *Prediction Refinement* module via tree-energy loss [21] for self-supervised learning in the training phase.

[26], [30]–[45] focus on effective multimodal feature fusion, which can be achieved via implicit multimodal feature aggregation, or explicit modal contribution evaluation [5], [46]. Given that depth can be noisy, one main direction exists to explore depth contribution [47], [48], which aims to distill the more informative depth for effective multimodal learning. For instance, [24] proposed to calibrate the potential noise in depth and a cross reference module was introduced to fuse the calibrated depth with the RGB features. [25] built the depth decompose module to filter noise in RGB images using the geometric prior of the depth map. With the same goal, alternative strategies usually involve an auxiliary depth estimation module [49] or refinement module [9] via self-supervised learning to achieve better utilization of the geometric information. Besides the deterministic RGB-D saliency detection models, generative model based saliency detection [50] is also explored to explain the “subjective nature” of saliency.

**Weakly-supervised Saliency Detection:** The primary weak annotations for saliency detection include image or class level label [6]–[11], [51], saliency subitizing [52], scribble [12]–[14], bounding box [15], and noisy labels from handcrafted-feature based methods [53]–[60]. Given the close relation between fixation prediction and salient object detection, [61] treats fixation maps as weak annotations for video salient object detection. Point supervision is used in [62] for video saliency detection. Based on class-activation map [63], Image-level supervision [6]–[8], [51] provide coarse foreground localization, highlighting the discriminative region of the object(s). Differently, scribble supervision [12]–[14] is usually accurate and sparse. Although bounding-box [15] usually cover the entire extend of the salient foreground, the extra background region leads to extensive false positive, especially for objects with concave shapes. Alternatively, noise labeling based solutions [55], [58]–[60] are designed to identify clean supervisions from labels generated with the conventional techniques.

**Graph-based Saliency Detection:** Graph-based [64]–[67] segmentation techniques usually represent an image as an undirected graph  $G = (\mathcal{V}, \mathcal{E})$ , where vertices  $v_i \in \mathcal{V}$  cor-

responds to pixels, and the edges  $(v_i, v_j) \in \mathcal{E}$  connect the neighborhood pixels. A weight  $w(v_i, v_j)$  is associated with each edge that connects a pair of vertices, which is a non-negative measure of the dissimilarity between  $v_i$  and  $v_j$ . Conventional graph-based segmentation methods [64] define the weight based on the intensity difference of the vertices pairs to achieve a partition of  $\mathcal{V}$  with different components. Given that graph-based methods can explore pixel-wise correlation, many conventional saliency detection models [68]–[74] construct pixel or superpixel level graph for an image to achieve salient region segmentation, where the weight is defined based on low-level image feature, *e.g.* color, intensity, location and *etc.* Graph can also be constructed based on deep features [21], [75]–[77] to explore image-wise correlation, leading to graph-based co-saliency detection models [78]–[82], video saliency detection [83].

**Multimodal Mutual Information Estimation:** Mutual Information (MI) captures the dependencies [84] between variables. For a pair of random variables  $X$  and  $Y$ , their MI  $I(X; Y)$  is defined as the KL-Divergence of the joint distribution  $p(X, Y)$  from the product of the marginal distributions  $p(X)$  and  $p(Y)$ . Due to its explicit dependency modeling ability, MI is typically used as a regularizer to encourage or limit the dependency between variables via MI maximization with a lower bound [85], [86] or MI minimization with an upper bound [16]. The MI maximization is usually applied for effective self-supervised representation learning [87]–[93], assuming each modality contains full information of the target distribution. On the contrary, the MI minimization [16], [17], [94], [95] acknowledge the partial information about the desired task within each modality, and it serves as a regularizer to achieve disentangled representation learning [22]. Mutual information can also be estimated via Bayesian analysis [96]–[98], which involves a prior probability and a likelihood to compute a posterior probability. Specifically, let’s define the mutual information of random variable  $x$  and  $y$  as  $I(x, y)$ , which can also be explained as the Kullback–Leibler divergence between the joint distribution  $p(x, y)$  and the outer product

of the marginal distribution  $p(x)$  and  $p(y)$ . Given samples  $D$  from the joint distribution, with Bayesian analysis, we have a prior  $p(I(x, y))$ , and a likelihood  $p(D|I(x, y))$ , the posterior expectation of the mutual information can be estimated via Bayesian analysis, achieving mutual information estimation.

### Prediction Refinement for Weakly-supervised Learning:

Considering that weak supervisions are used instead of the full annotations, prediction refinement is widely adopted in weakly-supervised models either during training [99], [100], or as post-processing [100]–[103] technique to obtain more accurate predictions. Among those methods, new supervisions are usually added manually [14], [99] to the model as pseudo labels. [99] introduced the newly annotated pixels to optimize model predictions during training via uncertainty-aware learning. [102] used class activation map (CAM) [63] as seed to generate initial predictions, which are then refined with denseCRF [29]. Similarly, [101], [103] generated coarse CAM and used seed refinement methods [104], [105] to produce better pseudo labels. [100] utilized denseCRF [29] to refine the prediction, where denseCRF [29] served as both training-phase refinement technique and post-processing method.

## III. OUR METHOD

Our weakly-supervised training dataset is  $D = \{X_i, y_i\}_{i=1}^N$ , where  $i$  indexes the samples and we omit it when it's clear,  $X = \{x^r, x^d\}$  is the input RGB ( $x^r$ ) and depth ( $x^d$ ) pair,  $y_s$  is the scribble annotation. We first design asymmetric feature extractors with a simple encoder to extract features for the input data pair and generate our initial prediction, where the asymmetric feature extractors are proven more effective than the conventional symmetric feature extractors. Then, the initial prediction is further refined during training with the minimum spanning tree based tree-energy loss and attention based fusion module (Sec. III-A). To achieve disentanglement representation learning for our multimodal task, we perform mutual information minimization with a tighter mutual information upper bound (Sec. III-B). Finally, we present a multimodal variational auto-encoder based prediction refinement strategy [18]–[20] (Sec. III-D), which is proven relatively robust to labeling noise compared with other deterministic prediction refinement techniques [29] and self-training [14].

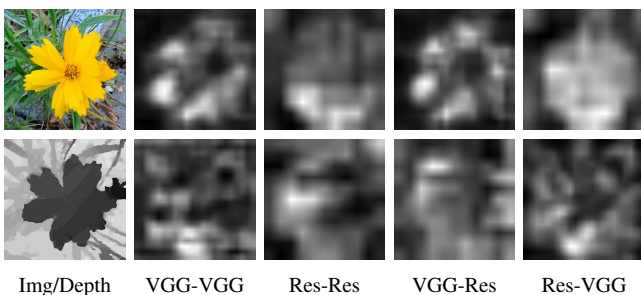


Fig. 2. Feature activation with different backbone settings. From left to right: RGB, Depth pair, activation of RGB (top), depth (bottom) within VGG-VGG, ResNet-ResNet, VGG-ResNet, and ResNet-VGG settings, where left means backbone for RGB, and the right one indicates backbone for depth.

### A. Initial Predictions via Asymmetric Encoders

**Asymmetric Encoders:** We discovered that the RGB image and depth data respond differently to the same backbone, where the ResNet50 backbone works better in generating more reliable foreground activation for RGB image, and the VGG16 backbone provides better activation for the depth data. In Fig. 2, we visualize the backbone feature (the deep level backbone feature) by performing channel-wise sum and min-max normalization. We observe that under our RGB-D SOD setting, the VGG backbone features focus more on details while ResNet backbone features highlight more target region(s). With the asymmetric encoders, semantic meaningful activation can be extracted from the RGB branch, and at the same time, we obtain structure accurate activation from the depth branch. In this paper, we utilized the pre-trained ResNet50 backbone to extract the RGB image features and the pre-trained VGG network to extract the depth features, where the former is defined as  $F_r = E_{res}(x^r)$  and the latter is defined as  $F_d = E_{vgg}(x^d)$ , where  $E_{res}(\cdot)$  and  $E_{vgg}(\cdot)$  indicate the ResNet50 and VGG16 backbone based feature extractors, respectively.

**Initial prediction generation:** For RGB and depth branch, we use a simple decoder to generate initial predictions with coarse features via  $\{s_{init}^r, f_{info}^r\} = D_{res}(F_r)$ , where  $D_{res}$  represents decoder for the ResNet50 backbone, consisting of four  $3 \times 3$  convolutional layers with four sets of feature fusion modules from [106].  $s_{init}^r, f_{info}^r$  are the prediction and the corresponding coarse feature. To achieve multimodal fusion, we simply concatenate the backbone feature of RGB image and depth data, and feed each stage of the backbone feature to a fusion module to achieve the fused RGB-D data based backbone feature  $F_{rgb-d} = Fu(F_r, F_d)$ , where  $Fu(\cdot)$  represents a fusion module consisting of channel-wise concatenation operation and one  $3 \times 3$  convolutional layers for each stage of the backbone feature as shown in Fig. 3. Note that VGG16 has five stages of backbone features, while ResNet50 has only four. Thus we duplicate the highest level feature from the RGB encoder, leading to five stages of features for  $F_{rgb-d}$ , which is precisely the same size and similar degree of semantic information as the depth backbone features as shown in Fig. 4. Based on it, we define the RGB-D prediction as  $\{s_{init}^{rgb-d}, f_{info}^{rgb-d}\} = D_{vgg}(F_{rgb-d})$ , where  $D_{vgg}$  represents the decoder for VGG backbone, which is composed of five  $3 \times 3$  convolutional layers with five sets of feature fusion modules from [106].  $s_{init}^{rgb-d}, f_{info}^{rgb-d}$  are the coarse prediction and the corresponding feature.

**Training-time prediction refinement:** As our scribble annotation is very sparse, directly training with it as supervision is insufficient to recover the image structure information. We draw on the approach in [21] to optimize predictions using input RGB images with high-dimensional features for self-supervised learning. To establish a point-to-point association, the image and features are first transformed into an undirected graph  $G = (V, E)$ , where  $V$  is the set of vertices consisting of all pixels in the image and  $E$  denotes the set of edges consisting of the weights of adjacent vertices. The weight between pixels are obtained by calculating the  $L2$  distance

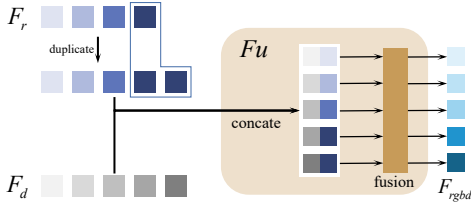


Fig. 3. Illustration of the feature fusion module  $Fu$  for Asymmetric Encoder features. The RGB backbone feature  $F_r$  is duplicated to the same channel size with depth feature  $F_d$ .  $Fu$  consists of channel-wise concatenation and one  $3 \times 3$  convolutional layers for each backbone feature stage.

as  $\omega_{u,v}^k = \omega_{v,u}^k = |I_k(u) - I_k(v)|^2$ , where  $k$  indexes the high/low level features, including coarse features (high-level feature) and the raw input image (low-level feature),  $u, v$  are the index of the pixel, and  $I_k(u)$  represent the  $k^{th}$  feature of pixel  $u$ .

Following [21], the minimum spanning tree (MST) is calculated to obtain the distance of the shortest path ( $\mathbb{E}^k$ ) between vertices, with which the distance map of the MST is defined as  $D_{u,v}^k = D_{v,u}^k = \sum_{(u',v') \in \mathbb{E}_{u,v}^k} \omega_{u',v'}^k$ . The corresponding positive affinity matrices are obtained via:  $A(k) = \exp(-D^k/\sigma)$ , where  $\sigma$  is used to control the information intensity of  $k$ . We set  $\sigma = 0.02$  when  $k$  is the RGB image, and  $\sigma = 1$  when  $k$  is the high-level feature.

With the affinity matrices, the optimized prediction is obtained via cascaded low/high level filtering:

$$\begin{aligned} s_{ref}^r &= \mathbb{F}(A(f_{info}^r), \mathbb{F}(A(x^r), s_{init}^r)), \\ s_{ref}^{rgbd} &= \mathbb{F}(A(f_{info}^{rgbd}), \mathbb{F}(A(x^r), s_{init}^{rgbd})), \end{aligned} \quad (1)$$

where  $\mathbb{F}(A, s) = \frac{1}{z} \sum_v A_{u,v} s_v$  is the filtering function, which performs the normalized ( $z = \sum_v A_{u,v}$ ) weight sum across all pixels. Based on the refined prediction,  $L1$  loss is utilized between initial and refined predictions to encourage the unlabeled pixels into model updating via:

$$\begin{aligned} \mathcal{L}_{tree}^r &= \frac{1}{\Omega_U} \sum_{\forall u \in \Omega_U} |s_{init}^r(u) - s_{ref}^r(u)|, \\ \mathcal{L}_{tree}^{rgbd} &= \frac{1}{\Omega_U} \sum_{\forall u \in \Omega_U} |s_{init}^{rgbd}(u) - s_{ref}^{rgbd}(u)|, \end{aligned} \quad (2)$$

where  $\Omega_U$  represents the unlabeled set,  $s_{init}^r(u)$  is the prediction at location  $u$ .

### B. Mutual Information Optimization

With tree-energy loss [21] as an auxiliary loss function, we aim to achieve training-time prediction refinement. Further, as a typical multimodal learning task, we claim that effective multimodal representation learning is especially important for our task. Given RGB feature  $f_{info}^r$ , and RGB-D feature  $f_{info}^{rgbd}$ , we aim to explicitly maximize the contribution of depth for RGB-D saliency detection. In this case, we resort to mutual information minimization, which is optimized when  $f_{info}^{rgbd}$  contains minimal information from the RGB branch, thus we can maximize the contribution of depth. This operation is reasonable as  $f_{info}^{rgbd}$  by nature contains extensive information

### Algorithm 1 The First Stage Training Procedure

**Input:** Training dataset  $D = \{X_i, y_i\}_{i=1}^N$ , where  $X = \{x^r, x^d\}$ , and maximal number of iterations  $T$ .

**Output:** Parameters for encoder  $E_{vgg}$ ,  $E_{res}$ , decoder  $D_{vgg}$ ,  $D_{res}$ , fusion module  $Fu$ , and Mutual Information Optimization module.

- 1: Initialize encoder  $E_{vgg}$  with VGG16-Net [107], encoder  $E_{res}$  with ResNet50 [108], and other parameters by default.
- 2: **for**  $t \leftarrow 1$  to  $T$  **do**
- 3: Extract RGB features  $F_r = E_{res}(x^r)$  and depth features  $F_d = E_{vgg}(x^d)$ ;
- 4: Generate coarse prediction and corresponding feature  $s_{init}^r, f_{info}^r = D_{res}(F_r)$  for RGB branch;
- 5: Perform feature fusion using the fusion module: duplicate the highest level of  $F_r$  to generate  $F_r'$ , and obtained the fused RGB-D feature  $F_{rgbd} = Fu(F_r', F_d)$ .
- 6: Generate RGB-D prediction and information feature  $s_{init}^{rgbd}, f_{info}^{rgbd} = D_{vgg}(F_{rgbd})$ ;
- 7: Perform training-time prediction refinement (Eq. 1);
- 8: Obtain mutual information estimator (Eq. 6);
- 9: Update all parameters via Eq. 7.
- 10: **end for**

from  $f_{info}^r$ . By pushing them apart, depth contribution can be maximized.

Let  $X$  and  $Y$  be a pair of random variables, their mutual information  $I(X; Y)$  is defined as:

$$I(X; Y) = \mathbb{E}_{p(x,y)} \left[ \log \frac{p(x,y)}{p(x) \otimes p(y)} \right], \quad (3)$$

which is the Kullback-Leibler divergence of the joint distribution  $p(x, y)$  from the the product of the marginal distributions  $p(x)$  and  $p(y)$ . As mutual information measures the information that the two variables share, it is typically used as a regularizer in the loss function to encourage (via mutual information maximization) or limit dependency (via mutual information minimization) between variables. As the log density ratio between the joint distribution  $p(x, y)$  and product of marginals  $p(x) \otimes p(y)$  is intractable, mutual information is usually estimated instead of computed directly.

In this paper, given RGB-D feature  $x = f_{info}^{rgbd}$  and the RGB feature  $y = f_{info}^r$ , we aim to minimize their mutual information, achieving disentangled representation learning. To achieve this, we adopt vCLUB upper bound [16] of mutual information. Given  $X$  and  $Y$  with unknown conditional distribution  $p(y|x)$  (or  $p(x|y)$ ), [16] introduces contrastive log-ratio upper bound (CLUB) of mutual information between  $X$  and  $Y$ , which is defined as:

$$\begin{aligned} I_{vCLUB} &= \mathbb{E}_{p(x,y)} [\log q_\theta(y|x)] - \mathbb{E}_{p(x)} \mathbb{E}_{p(y)} [\log q_\theta(y|x)] \\ &\geq I(X; Y), \end{aligned} \quad (4)$$

$q_\theta(y|x)$  is a variational distribution with parameters  $\theta$  to approximate the true distribution  $p(y|x)$ , which is also called the ‘‘approximation network’’. As Eq. (4) involves sampling from both marginal distributions, leading to  $\mathcal{O}(N^2)$  computational complexity, where  $N$  is the size of the samples.

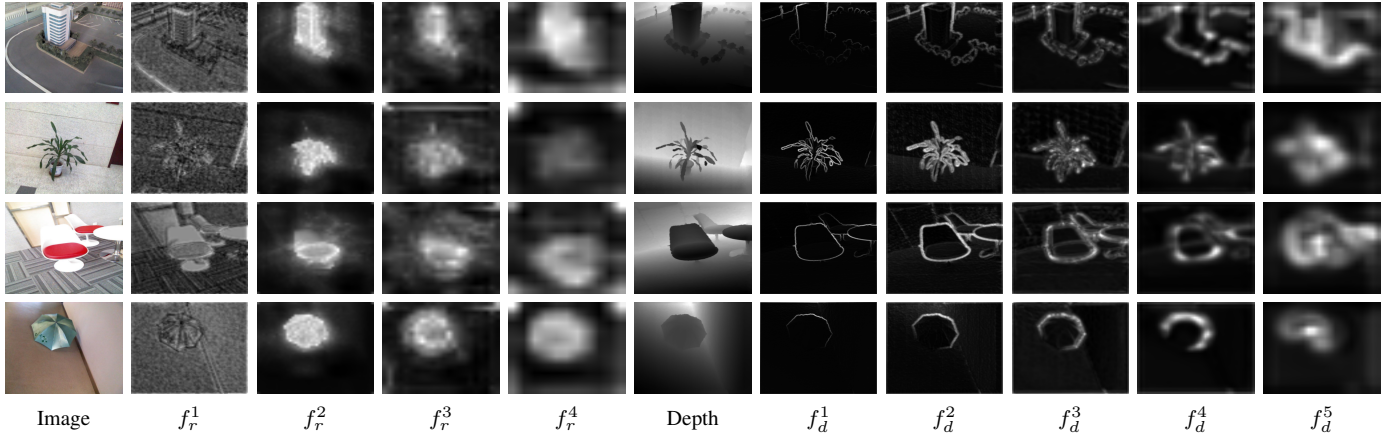


Fig. 4. Visualization of our proposed asymmetric encoder produces the RGB and depth activation maps.  $f_r^i$ ,  $i = 1, \dots, 4$  is the RGB (ResNet) backbone feature, and  $f_d^i$ ,  $i = 1, \dots, 5$  means the depth (VGG) backbone feature.

To accelerate the mutual information upper bound computation, [16] uniformly sample negative pairs  $(x_i, y_{k'_i})$ , treating its probability  $q_\theta(y_{k'_i}|x_i)$  as unbiased estimation of the mean of the probability  $\mathbb{E}_{p(y)}[q_\theta(y|x_i)]$ . In this case, the sampled mutual information estimator [16] is defined as:

$$I_{vCLUBs} = \frac{1}{N} \sum_{i=1}^N [\log q_\theta(y_i|x_i) - \log q_\theta(y_{k'_i}|x_i)], \quad (5)$$

where  $N$  is the size of the training data, or the minibatch.

*Technical details:* The approximation network  $q_\theta(y|x)$  is modeled with Gaussian distribution following [16], where we define  $q_\theta(y|x) = \mathcal{N}(y; \mu(x), \sigma^2(x))$ . We model  $\mu(x)$  with two fully connected layers with a ReLU activation function in the between. We model  $\log(\sigma^2(x))$  instead of  $\sigma^2(x)$  for stable training, which shares the same structure as  $\mu(x)$ , except that we add an extra Tanh activation function at the end of  $\log(\sigma^2(x))$  to produce a relatively narrow Gaussian distribution. We define the corresponding RGB feature and RGB-D image as positive pair, and the non-corresponding pair as negative pair for the computation of the sampled mutual information estimator in Eq. (5). We perform RGB-D to RGB feature transformation via  $q_\theta(f_{info}^r | f_{info}^{rgbd})$ , achieving mutual information estimator via:

$$I_{mi} = I_{vCLUBs}(f_{info}^{rgbd}, f_{info}^r). \quad (6)$$

### C. Objective Function of the First Stage Training

We first define partial cross-entropy loss [109] between each of the initial predictions and the scribble ground truth with only labeled pixels used, leading to  $\mathcal{L}_{pce}(s_{init}^{rgbd}, y)$  and  $\mathcal{L}_{pce}(s_{init}^r, y)$ , where  $y$  in this case represents the combination of the foreground scribble and background scribble. Then, tree-energy loss in Eq. (2) is incorporated to encourage the contribution of unlabeled pixels. Lastly, the mutual information regularization in Eq. (6) is used to explicitly model the contribution of depth for RGB-D saliency detection. Our final loss function is then defined as:

$$\mathcal{L} = \mathcal{L}_r + \mathcal{L}_{rgbd} + \alpha I_{mi}, \quad (7)$$

where  $\mathcal{L}_r$  means the RGB branch loss, which defined as  $\mathcal{L}_r = \mathcal{L}_{pce}(s_{init}^r, y) + \mathcal{L}_{tree}^r$ , and RGB-D branch loss  $\mathcal{L}_{rgbd}$  is defined as  $\mathcal{L}_{rgbd} = \mathcal{L}_{pce}(s_{init}^{rgbd}, y) + \mathcal{L}_{tree}^{rgbd}$ . Empirically we set  $\alpha = 0.005$  to balance the contribution of the mutual information regularization term for stable training. We show the first training stage pipeline of our framework in Algorithm 1 for better understanding of the implementation details.

### D. Conditional Multimodal VAE as Refinement

Given dataset  $D = \{X_i, y_i\}_{i=1}^N$  as our training dataset, where  $i$  indexes the samples and we omit it when it's clear,  $X = \{x^r, x^d\}$  is the input RGB ( $x^r$ ) and depth ( $x^d$ ) pair,  $y$  is the ground truth saliency map. We present a conditional multimodal variational auto-encoder (VAE) [18]–[20] with explicit unimodal optimization for RGB-D latent representation learning.

**Conditional Unimodal VAE:** Following the maximum likelihood training pipeline, a conditional VAE (CVAE) is trained to maximize the conditional log-likelihood of individual datapoints  $\log p_\theta(y|X) = \sum_i \log p_\theta(y|x^i)$ . Unfortunately, the computation of  $p_\theta(y|x^i)$  involves integral over all configurations of latent variables  $z$ , which requires exponential time to compute. To achieve computationally tractable learning of the generative process, [18], [19] introduces a recognition model  $q_\phi(z|x, y)$  as an approximation of the intractable true posterior  $p_\theta(z|x, y)$ . The goal is then finding the variational parameters  $\phi$  that minimize the Kullback–Leibler (KL) divergence between the variational posterior  $q_\phi(z|x, y)$  and the true posterior  $p_\theta(z|x, y)$  as:

$$q_{\phi^*}(z|x, y) = \arg \min_{\phi} D_{KL}(q_\phi(z|x, y) || p_\theta(z|x, y)), \quad (8)$$

where the KL-divergence term can be decomposed:

$$\begin{aligned} D_{KL}(q_\phi(z|x, y) || p_\theta(z|x, y)) \\ = \mathbb{E}_{q_\phi(z|x, y)} \log q_\phi(z|x, y) - \mathbb{E}_{q_\phi(z|x, y)} \log \frac{p_\theta(z|x, y)}{p_\theta(x, y)}. \end{aligned} \quad (9)$$

Given  $p_\theta(x, y, z) = p_\theta(y|x, z)p_\theta(z|x)p(x)$ , we can further decompose the second expectation term in Eq. (9) as:

$$\begin{aligned} & \mathbb{E}_{q_\phi(z|x, y)} \log \frac{p_\theta(x, y, z)}{p_\theta(x, y)} \\ &= \mathbb{E}_{q_\phi(z|x, y)} \log \frac{p_\theta(y|x, z)p_\theta(z|x)p(x)}{p_\theta(x, y)} \quad (10) \\ &= \mathbb{E}_{q_\phi(z|x, y)} \log p_\theta(y|x, z) + \mathbb{E}_{q_\phi(z|x, y)} \log p_\theta(z|x) \\ &\quad - \log p_\theta(y|x). \end{aligned}$$

We take Eq. (10) back to Eq. (9) and obtain:

$$\begin{aligned} & D_{KL}(q_\phi((z|x, y)||p_\theta(z|x, y))) \\ &= \mathbb{E}_{q_\phi(z|x, y)} \log q_\phi(z|x, y) - \mathbb{E}_{q_\phi(z|x, y)} \log p_\theta(z|x) \\ &\quad - \mathbb{E}_{q_\phi(z|x, y)} \log p_\theta(y|x, z) + \log p_\theta(y|x) \\ &= \underbrace{D_{KL}(q_\phi(z|x, y)||p_\theta(z|x)) - \mathbb{E}_{q_\phi(z|x, y)} \log p_\theta(y|x, z)}_{-\text{ELBO}(x, y, \theta, \phi)} \\ &\quad + \log p_\theta(y|x). \quad (11) \end{aligned}$$

We simplify Eq. (11), and obtain:

$$\begin{aligned} & \log p_\theta(y|x) \\ &= \text{ELBO}(x, y, \theta, \phi) + D_{KL}(q_\phi(z|x, y)||p_\theta(z|x, y)). \quad (12) \end{aligned}$$

By Jensen's inequality,  $D_{KL}(q_\phi(z|x, y)||p_\theta(z|x, y))$  in Eq. (12) is always greater or equal to zero. In this case, minimizing it can be achieved by maximizing  $\text{ELBO}(x, y, \theta, \phi)$ , which is the evidence lower bound (ELBO). With the reparameterization trick [18], the KL-divergence term in Eq. (12) can be solved in closed-form given that both the prior and posterior are Gaussian.

**Conditional Multimodal VAE:** In our multimodal setting, we obtain the same derivation as in Eq. (12), except that we change  $x$  to  $X$ , representing the multimodal data, leading to ELBO of conditional multimodal VAE as:

$$\begin{aligned} & \text{ELBO}(X, y, \theta, \phi) \\ &= \mathbb{E}_{q_\phi(z|X, y)} \log p_\theta(y|X, z) - D_{KL}(q_\phi(z|X, y)||p_\theta(z|X)), \quad (13) \end{aligned}$$

where  $q_\phi(z|X, y)$  and  $p_\theta(z|X)$  represent the joint posterior and prior respectively. To achieve closed-form solution for the KL-divergence term in Eq. (13), MVAE [20] uses a product of experts (PoE) [110], [111] based on the reparameterization trick, namely the ‘‘prior expert’’ as estimation of the joint prior and ‘‘posterior expert’’ as estimation of the joint posterior. Specifically, when each of the experts is Gaussian, their product is still Gaussian, leading to a closed form solution for the KL-divergence term in Eq. (13). The product of the Gaussian expert will have mean  $\mu = (\sum_x \mu_x T_x)(\sum_x T_x)^{-1}$ , and covariance  $\Sigma = (\sum_x T_x)^{-1}$ , where  $\mu_x$  and  $\Sigma_x$  are the statistics of the Gaussian expert of modality  $x$ , and  $T_x = \Sigma_x^{-1}$  is the inverse covariance or the precision of the Gaussian expert with modality  $x$ . With the PoE based joint variational posterior/prior factorizing, we can solve the KL-divergence term in Eq. (13) in closed form.

**Joint Prior and Posterior via PoE:** For our conditional generation setting,  $X = \{x^r, x^d\}$ , including the appearance

information from the RGB image  $x^r$  and geometric information from the depth data  $x^d$ . The joint prior is then:

$$\begin{aligned} p(z|X) &= p(z|x^r, x^d) = \frac{p(x^r, x^d|z)p(z)}{p(x^r, x^d)} \\ &= \frac{p(z)}{p(x^r, x^d)} \prod_x p(x|z) \\ &= \frac{p(z)}{p(x^r, x^d)} \prod_x \frac{p(z|x)p(x)}{p(z)} \quad (14) \\ &= \frac{\prod_x p(z|x)}{p(z)} \cdot \frac{\prod_x p(x)}{p(x^r, x^d)} \\ &\propto \frac{\prod_x p(z|x)}{p(z)} \end{aligned}$$

In practice, the  $p(z|x)$  is approximated with  $p(z|x) = \hat{q}(z|x)p(z)$  to avoid the quotient term, leading to the final joint prior as:

$$p_\theta(z|X) \propto \frac{\prod_x p(z|x)}{p(z)} \approx p(z) \prod_x \hat{q}(z|x), \quad (15)$$

where  $\hat{q}(z|x)$  is modeled with a neural network, which is Gaussian. In this case, the joint prior is modeled with the product of Gaussian distributions, and PoE [110] is used to obtain the statistics of  $p_\theta(z|X)$ .

Similarly, the joint posterior  $q(z|X, y)$  is obtained via:

$$\begin{aligned} q(z|X, y) &= q(z|x^r, x^d, y) = \frac{p(x^r, x^d, y|z)p(z)}{p(x^r, x^d, y)} \\ &= \frac{p(z)}{p(x^r, x^d, y)} \prod_x p(x, y|z) \\ &= \frac{p(z)}{p(x^r, x^d, y)} \prod_x \frac{p(z|x, y)p(x, y)}{p(z)} \quad (16) \\ &= \frac{\prod_x p(z|x, y)}{p(z)} \cdot \frac{\prod_x p(x, y)}{p(x^r, x^d, y)} \\ &\propto \frac{\prod_x p(z|x, y)}{p(z)} \end{aligned}$$

We also approximate  $p(z|x, y)$  with  $p(z|x, y) = \hat{q}(z|x, y)p(z)$ , and define the joint posterior as:

$$p_\theta(z|X, y) \propto \frac{\prod_x p(z|x, y)}{p(z)} \approx p(z) \prod_x \hat{q}(z|x, y), \quad (17)$$

where  $\hat{q}(z|x, y)$  is Gaussian and modeled with a neural network, leading to the product of Gaussian distribution for the joint posterior distribution, which can be computed in closed form with PoE [110].

**Conditional Multimodal VAE as Refinement:** In order to refine the prediction and mitigate error propagation issues, we explore the potential of Conditional Multimodal VAE [20] and apply it to our weakly-supervised learning setting, leading to a two-stage training pipeline. Within the fully-supervised conditional VAE framework, the conditional variable  $x$  is used to produce the conditional prediction  $p(y|x, z)$ . Given our weakly supervised setting with scribble annotation, the label  $y$  is partial, directly modeling the posterior distribution  $q_\phi(z|x, y)$  is problematic. Instead, we use the pseudo label from the first step training as  $y$  in this case, and all the other

derivations are the same as the conditional multimodal VAE in Sec. III-D.

With the first stage of training, we obtain relatively reasonable predictions on the training dataset. However, we observe less accurate predictions happen along object boundaries, which can be refined by post-processing techniques, *i.e.* denseCRF [29] as shown in Fig. 5. However, the performance of denseCRF [29] relies on carefully picked hyper-parameters, making it not robust. According to the noise robustness learning [112], where adding noise to the network can prevent the model from overfitting, we introduce stochastic prediction refinement by adding structured noise via a conditional multimodal variational auto-encoder (CVAE) [18]–[20] as the second stage training, which is proven relatively robust to labeling noise, suffering less error propagation issues.

The goal of CVAE is finding the variational parameters  $\phi$  that minimize the Kullback–Leibler (KL) divergence ( $D_{\text{KL}}$ ) between the variational posterior  $q_\phi(z|X, y)$  and the true posterior  $p_\theta(z|X, y)$  via maximizing the conditional log-likelihood, which is usually achieved via optimizing the evidence lower bound (ELBO)<sup>1</sup>:

$$\begin{aligned} \text{ELBO}(X, y, \theta, \phi) = & \underbrace{\lambda \mathbb{E}_{q_\phi(z|X, y)} \log p_\theta(y|X, z)}_{\text{conditional generation}} \\ & - \beta D_{\text{KL}}(q_\phi(z|X, y) || p_\theta(z|X)), \end{aligned} \quad (18)$$

where  $\lambda$  and  $\beta$  are hyper-parameters to balance the two parts [113]. For our multimodal data setting, both the prior and posterior of  $z$  are based on the multimodal data  $X$ , which are defined as the “joint prior” and “joint posterior” respectively. We achieve them via product of experts (PoE) [110], [111], leading to both the “prior expert” as estimation of the “joint prior expert” and the “joint posterior expert”, which are both Gaussian. In this case, the KL-divergence term in Eq. (18) can be solved in closed form.

*Multimodal VAE as Refinement:* The multimodal VAE refinement process is based on the conditional VAE framework, where we use pseudo label  $s_{ref}^{rgb}$  from the first stage training as supervisions. We follow a simpler training pipeline than the first stage training, each modality has a ResNet50 encoder with a similar multimodal fusion  $F_u$  operation and the decoder for the ResNet50 backbone is used to generate the refined prediction. Further, we use the same structure neural network to obtain both the “prior expert” and “posterior expert”, and generate our prediction only for the RGB-D branch for simplicity. To obtain the “prior expert”  $p_\theta(z|X)$ , we follow PoE [110], [111] and obtain:

$$p_\theta(z|X) \propto \frac{\prod_x p(z|x)}{p(z)} \approx p(z) \prod_x \hat{q}(z|x), \quad (19)$$

where  $\hat{q}(z|x)$  is modeled with a neural network, which is Gaussian. In this case, the joint prior is modeled with the product of Gaussian distributions.

Similarly, the “posterior expert” can be obtained as:

$$p_\theta(z|X, y) \propto \frac{\prod_x p(z|x, y)}{p(z)} \approx p(z) \prod_x \hat{q}(z|x, y), \quad (20)$$

where  $\hat{q}(z|x, y)$  is Gaussian and modeled with a neural network, leading to the product of Gaussian distribution for the joint posterior distribution.

*PoE statistics computation:* Specifically, when each of the experts is Gaussian, their product is still Gaussian. The product of the Gaussian expert will have mean  $\mu = (\sum_k \mu_k T_k) (\sum_k T_k)^{-1}$ , and covariance  $\sigma^2 = (\sum_k T_k)^{-1}$ , where  $\mu_k$  and  $\sigma_k$  are the statistics of the Gaussian expert of modality  $k$ , and  $T_k = 1/\sigma_k^2$  is the inverse covariance or the precision of the Gaussian expert. With the PoE based joint variational posterior/prior factorizing, we can solve the KL-divergence term in Eq. (18) in closed form.

*Technical details:* Within both the prior expert in Eq. (19) and posterior expert in Eq. (20), we need to compute the unimodal prior and posterior respectively. In this paper, we design them using the same structure, which consists of five  $4 \times 4$  convolutional layers with batch normalization and Leaky Relu, and two linear layers with the same structure to obtain  $\mu$  and  $\log(\sigma^2)$  respectively. During training, the reconstruction loss (to maximize the log-likelihood of the conditional distribution in Eq. (18)) is defined as the pixel-wise structure-aware loss [127] between prediction from the RGB-D branch and the pseudo label  $s_{ref}^{rgb}$  as:

$$\begin{aligned} & \arg \max_{\theta, \phi} \mathbb{E}_{q_\phi(z|X, y)} \log p_\theta(y|X, z) \\ = & \arg \min_{\theta, \phi} \mathcal{L}(\mathbb{E}_{q_\phi(z|X, y)} [p_\theta(y|X, z)], s_{ref}^{rgb}) \end{aligned} \quad (21)$$

The KL-divergence loss within the ELBO in Eq. (18) is the divergence of the joint “posterior expert” from the joint “prior expert”, where we set  $\lambda = 1$  and  $\beta = 5$  with linear annealing for stable training [113]. Note that, for the generation process, latent code is involved. We adjust the previous decoder for ResNet50 to take the latent code as input, where we simply tile the latent code to the same size as the top level feature, and concatenate them, which is then fed to another  $3 \times 3$  convolution layer to obtain the new top level feature of the same size as the previous one. The other structure is the same as the decoder for the ResNet50 backbone discussed in Sec. III-A.

## IV. EXPERIMENTAL RESULTS

**Dataset:** For fair comparisons with existing RGB-D saliency detection models, we follow the conventional training setting, in which the training set is a combination of 1,485 images from the NJU2K dataset [3] and 700 images from the NLPR dataset [4]. We then test the performance of our model and competing models on the NJU2K testing set, NLPR, testing set LFS [119], DES [30], SSB [118] SIP [120] and DUT [34] testing set.

**Evaluation Metrics:** We evaluate the performance of the models on four golden evaluation metrics, *i.e.* Mean Absolute Error ( $\mathcal{M}$ ), Mean F-measure ( $F_\beta$ ), Mean E-measure ( $E_\xi$ ) [128] and S-measure ( $S_\alpha$ ) [129].

**Implementation Details:** Our model is implemented using *Pytorch*. For the first training stage, the RGB encoder is initialized with ResNet50 [108] backbone and the depth encoder is initialized with VGG16-Net [107]. Both of the two backbones

<sup>1</sup>The complete derivation is provided in the supplementary material

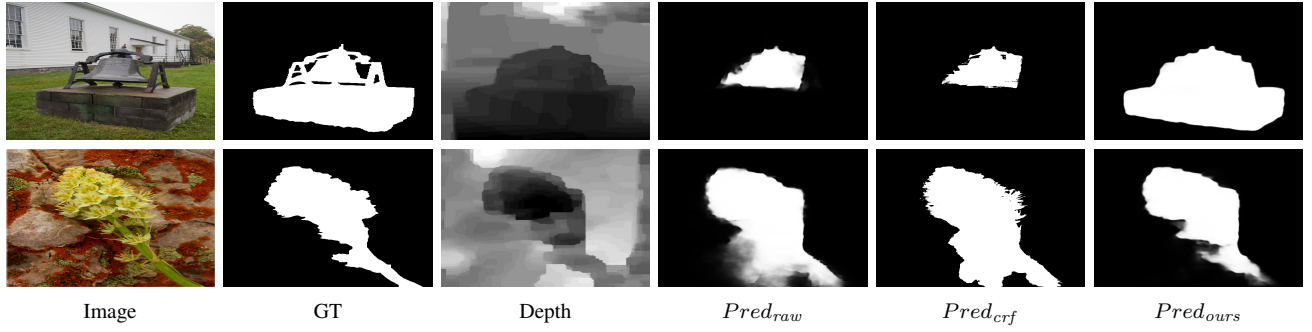


Fig. 5. Prediction comparison, where “Image”, “GT” and “Depth” are the RGB image, the ground truth map, and the depth map. “ $Pred_{raw}$ ”, “ $Pred_{crf}$ ” and “ $Pred_{ours}$ ” represent prediction after the first stage training, refinement with denseCRF [29] and the proposed Conditional Multimodal VAE, respectively.

TABLE I  
BENCHMARKING RESULTS OF SOD MODELS.  $\uparrow$  &  $\downarrow$  DENOTE THE LARGER AND SMALLER IS BETTER, RESPECTIVELY AND “BKB”: THE BACKBONE. V16, R50, PVTv2 AND SWIN ARE VGG16, RESNET50, PVTv2 [114] AND SWIN [115] BACKBONES, RESPECTIVELY. MOB: MOBILENETV2 BACKBONE [116]. CNN: THE BACKBONE FROM [33] WITH SIX HIERARCHIES. 3DC: THE BACKBONE FROM [28] WITH 3D CONVOLUTIONS. ViT: T2T-ViT BACKBONE [117].

Method	Year	BKB	NJU2K [3]				SSB [118]				DES [30]				NLPR [4]				LFSD [119]				SIP [120]			
			$S_\alpha \uparrow$	$F_\beta \uparrow$	$E_\xi \uparrow$	$M \downarrow$	$S_\alpha \uparrow$	$F_\beta \uparrow$	$E_\xi \uparrow$	$M \downarrow$	$S_\alpha \uparrow$	$F_\beta \uparrow$	$E_\xi \uparrow$	$M \downarrow$	$S_\alpha \uparrow$	$F_\beta \uparrow$	$E_\xi \uparrow$	$M \downarrow$	$S_\alpha \uparrow$	$F_\beta \uparrow$	$E_\xi \uparrow$	$M \downarrow$	$S_\alpha \uparrow$	$F_\beta \uparrow$	$E_\xi \uparrow$	$M \downarrow$
Early Fusion Models																										
DANet [31]	2020	V16	.897	.877	.926	.046	.892	.857	.915	.048	.905	.848	.961	.028	.908	.850	.945	.031	.845	.826	.872	.082	.878	.829	.914	.054
UCNet [50]	2020	R50	.897	.886	.930	.043	.903	.884	.938	.039	.934	.919	.967	.019	.920	.891	.951	.025	.864	.855	.901	.066	.875	.867	.914	.051
JLDCF [33]	2020	CNN	.902	.885	.935	.041	.903	.873	.936	.040	.931	.907	.959	.021	.925	.894	.955	.022	.862	.848	.894	.070	.880	.873	.918	.049
RD3D [28]	2021	3DC	.927	.909	.943	.033	.914	.881	.932	.039	.950	.923	.968	.017	.933	.898	.953	.022	-	-	-	-	.892	.881	.917	.046
Late Fusion Models																										
AFNet [48]	2019	V16	.822	.827	.867	.077	.825	.806	.872	.075	.770	.713	.809	.068	.799	.755	.851	.058	.738	.736	.796	.134	.720	.702	.793	.118
A2dele [32]	2020	V16	.873	.867	.913	.051	.876	.874	.925	.044	.881	.868	.913	.030	.887	.871	.933	.031	.831	.829	.872	.076	.826	.827	.887	.070
Cross-level Fusion Models																										
MSal [38]	2021	Mob	.910	.891	.939	.039	.903	.874	.930	.041	.929	.908	.957	.021	.920	.885	.950	.025	.847	.825	.879	.080	.873	.861	.908	.053
DSA2F [25]	2021	V19	.903	.901	.923	.039	.904	.898	.933	.036	.920	.896	.962	.021	.918	.897	.950	.024	.882	.878	.919	.055	-	-	-	-
VST [121]	2021	ViT	.922	.898	.939	.035	.913	.879	.937	.038	.943	.920	.965	.017	.932	.897	.951	.024	.890	.871	.917	.054	.904	.894	.933	.040
GTSOD [122]	2021	Swin	.929	.924	.956	.028	.916	.898	.950	.032	.945	.928	.971	.016	.938	.921	.966	.018	.872	.862	.901	.066	.906	.908	.940	.037
C2DF [123]	2022	R50	.908	.898	.936	.038	.902	.881	.936	.038	.921	.908	.945	.020	.927	.904	.955	.021	.863	.859	.897	.065	.871	.865	.912	.053
SSLSOD [23]	2022	V16	.902	.887	.929	.043	.886	.867	.921	.048	.933	.919	.966	.019	.914	.881	.941	.027	-	-	-	-	.870	.862	.900	.059
CLNet [5]	2021	R50	.939	.925	.956	.032	.921	.895	.959	.034	.953	.926	.970	.015	.941	.909	.964	.019	.877	.862	.911	.064	.894	.887	.933	.044
DCF [24]	2022	R50	.890	.880	.924	.045	.886	.870	.926	.044	.895	.868	.924	.026	.907	.878	.941	.028	.807	.801	.842	.094	.848	.841	.892	.067
CIRNet [124]	2022	R50	.901	.880	.917	.047	.901	.872	.914	.046	.906	.871	.913	.029	.920	.881	.937	.028	.822	.803	.834	.096	.861	.840	.886	.069
Weak/Un-supervised Models																										
SSOD [14]	2022	V16	.899	.878	.922	.044	.887	.851	.914	.044	.916	.887	.939	.029	.913	.874	.936	.028	.832	.814	.860	.085	.865	.841	.900	.056
DSU [59]	2022	R50	.734	.693	.752	.133	.797	.759	.826	.097	.826	.764	.828	.061	.809	.739	.836	.064	.780	.761	.795	.128	.693	.613	.734	.155
WSSOD [13]	2020	V16	.851	.840	.905	.062	.860	.843	.915	.054	.858	.840	.918	.039	.872	.842	.925	.038	.821	.821	.871	.087	.811	.795	.868	.082
SCWS [12]	2021	R50	.843	.822	.896	.065	.841	.808	.895	.064	.862	.835	.919	.035	.868	.827	.916	.042	.794	.776	.845	.103	.825	.792	.885	.074
JSM [125]	2021	R50	.724	.689	.746	.130	.790	.758	.822	.093	.826	.772	.823	.056	.810	.749	.841	.059	.766	.756	.790	.128	.707	.640	.740	.142
DLM [126]	2022	PVTv2	.808	.765	.837	.097	.833	.790	.869	.079	.833	.749	.871	.060	.796	.668	.811	.081	.824	.807	.851	.098	.777	.727	.830	.109
Ours	2022	RV	.890	.880	.929	.046	.891	.873	.934	.042	.928	.921	.965	.019	.914	.895	.953	.025	.849	.844	.889	.072	.876	.863	.924	.049

TABLE II  
CROSS-MODEL FUSION ANALYSIS BY COMPARING WITH BOTH THE BASE RGB MODEL AND BASE RGB-D MODEL VIA EARLY-FUSION.

Method	NJU2K [3]				SSB [118]				DES [30]				NLPR [4]				LFSD [119]				SIP [120]			
	$S_\alpha \uparrow$	$F_\beta \uparrow$	$E_\xi \uparrow$	$M \downarrow$	$S_\alpha \uparrow$	$F_\beta \uparrow$	$E_\xi \uparrow$	$M \downarrow$	$S_\alpha \uparrow$	$F_\beta \uparrow$	$E_\xi \uparrow$	$M \downarrow$	$S_\alpha \uparrow$	$F_\beta \uparrow$	$E_\xi \uparrow$	$M \downarrow$	$S_\alpha \uparrow$	$F_\beta \uparrow$	$E_\xi \uparrow$	$M \downarrow$	$S_\alpha \uparrow$	$F_\beta \uparrow$	$E_\xi \uparrow$	$M \downarrow$
$B_{rgb}$	.810	.782	.878	.079	.820	.786	.892	.070	.784	.722	.858	.062	.815	.749	.893	.054	.740	.728	.815	.127	.784	.745	.866	.089
$B_{rgb-d}$	.809	.785	.877	.080	.801	.758	.876	.080	.846	.797	.924	.043	.822	.757	.897	.051	.785	.775	.852	.104	.786	.758	.869	.089
$C_{rgb-d}$	.839	.807	.894	.068	.831	.783	.890	.070	.873	.825	.929	.035	.842	.769	.905	.048	.792	.773	.843	.110	.822	.793	.889	.075

are initialized with the corresponding parameters trained on ImageNet [130]. We set the maximum epoch as 30, and the initial learning rate as  $3 \times 10^{-5}$ . For the VAE refinement stage, both encoders are initialized with ResNet50 [108], and set the maximum epoch as 50, and the initial learning rate is  $2.5 \times 10^{-5}$ . The other newly added layers are initialized by

default. For both stages, We resize all the images and ground truth to the same spatial size of  $352 \times 352$  pixels. We adopt the “step” learning rate decay policy, and set the decay size as 1 and decay rate as 0.95. The models are trained with batch size 3 on an NVIDIA GeForce RTX 3090 GPU, and the training takes 5.5 hours, VAE refinement stage takes 7.5



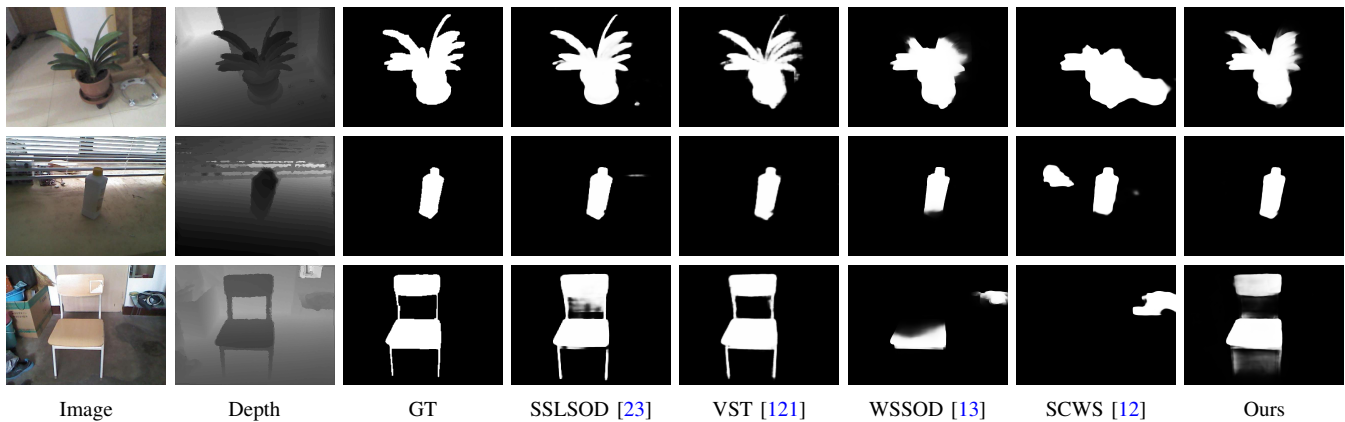


Fig. 6. Visualization of the generated saliency maps from benchmark RGB-D saliency detection models and ours.

TABLE III  
BACKBONE ANALYSIS TO VERIFY THE EFFECTIVENESS OF THE PROPOSED ASYMMETRIC FEATURE EXTRACTORS.

Method	NJU2K [3]				SSB [118]				DES [30]				NLPR [4]				LFSD [119]				SIP [120]			
	$S_\alpha \uparrow$	$F_\beta \uparrow$	$E_\xi \uparrow$	$\mathcal{M} \downarrow$	$S_\alpha \uparrow$	$F_\beta \uparrow$	$E_\xi \uparrow$	$\mathcal{M} \downarrow$	$S_\alpha \uparrow$	$F_\beta \uparrow$	$E_\xi \uparrow$	$\mathcal{M} \downarrow$	$S_\alpha \uparrow$	$F_\beta \uparrow$	$E_\xi \uparrow$	$\mathcal{M} \downarrow$	$S_\alpha \uparrow$	$F_\beta \uparrow$	$E_\xi \uparrow$	$\mathcal{M} \downarrow$	$S_\alpha \uparrow$	$F_\beta \uparrow$	$E_\xi \uparrow$	$\mathcal{M} \downarrow$
$r\_d(RV)$	.852	.827	.906	.063	.845	.803	.900	.066	.900	.858	.949	.033	.865	.810	.922	.042	.802	.779	.847	.106	.839	.815	.902	.067
$rR\_dR$	.849	.817	.896	.066	.843	.793	.894	.068	.898	.860	.944	.031	.861	.796	.916	.042	.798	.771	.836	.112	.844	.816	.901	.067
$rV\_dR$	.838	.805	.894	.070	.829	.778	.885	.071	.881	.827	.936	.035	.844	.772	.903	.047	.781	.752	.831	.113	.827	.791	.891	.073
$rV\_dV$	.836	.802	.893	.068	.832	.786	.893	.068	.870	.818	.932	.038	.833	.756	.895	.050	.789	.765	.842	.111	.817	.784	.886	.077

hours. The features and predictions were optimized by the holistic attention [131] to obtain finer predictions that were also generated in each mode, but were omitted for brevity.

### A. Performance comparison

**Quantitative comparison:** We compare our method with state-of-the-art fully-supervised and weakly-supervised RGB-D saliency detection models, and show performance in Table I. As a comparison method, DSU [59] is an unsupervised method that disentangles the saliency regions from the depth and RGB images. JSM [125] uses the traditional SOD algorithm as a pseudo-label and updates the annotation with the help of semantic labels. SCWS [12], SSOD [14] and WSSOD [13] are based on scribble annotations. The results show that we achieve the best results on 5/6 dataset, except the NJU2K dataset [3]. The reason is that our mutual information optimization may accidentally encourage noisy depth for the final prediction. Note that both WSSOD [13] and SCWS [12] are RGB saliency detection models with scribble supervision. We directly perform early fusion and introduce another  $3 \times 3$  convolutional layers to map the RGB-D data to 3 channel feature map to fit their original implementations.

**Qualitative comparison:** We also show the generated saliency maps of our method and existing techniques in Fig. 6. It can be observed that our model makes effective use of depth information and learns more details than other weakly supervised methods.

### B. Ablation Studies

Unless stated otherwise, we define the output from the RGB-D branch as model prediction.

**Base models:** We train two base models with only RGB image used ( $B_{rgb}$ ) or both RGB-D data ( $B_{rgbd}$ ) used for weakly-supervised RGB-D saliency detection with partial cross-entropy loss. Specifically, we use the same ResNet50 encoder and decoder and ResNet50 as discussed in Sec. III-A. For  $B_{rgbd}$ , early fusion is used to fuse RGB and depth at the input, and an extra  $3 \times 3$  convolutional layer is used to map the concatenated feature to a 3-channel feature map, which will then be fed to the encoder-decoder framework. Performance is shown in Table II, which explains that early fusion can be effective to some extent, especially for DES, NLPR, and LFSD datasets, verifying the effectiveness of depth for RGB-D saliency detection.

**Cross-level fusion:** With the proposed simple cross-level fusion strategy as discussed in Sec. III-A, we obtain  $C_{rgbd}$ , and show its performance in Table II. The significant performance improvement verifies the effectiveness of our cross-level fusion strategy.

**Asymmetric feature extractor analysis:** We discovered that different backbones activate differently to the multimodal data. Based on the cross-level fusion model, we compare the backbone configurations for RGB and depth, and show model performance in Table III, the activation is shown in Fig. 2, where  $rR\_dR$  indicates ResNet50 backbone ( $R$ ) for both the RGB image ( $r$ ) and the depth  $d$ . The results show that the selection of a suitable backbone facilitates the integration of multimodal information. The performance improvement of  $r\_d(RV)$  compared to other methods demonstrates the effectiveness of our proposed asymmetric feature extractor. Note that we supervise the above model with partial cross-entropy loss.

**Graph based progressive refinement analysis:** To better

TABLE IV

MODULE EFFECTIVENESS ANALYSIS, INCLUDING THE PROGRESSIVE FUSION MODULE AND THE MUTUAL INFORMATION MINIMIZATION REGULARIZATION.  $r\_d$  MEANS THE BASELINE WITH THE ASYMMETRIC FEATURE EXTRACTOR (SAME AS  $r\_d(RV)$  IN TABLE III).  $pr\_rd$  MEANS THE RESULT OF THE GRAPH BASED PROGRESSIVE REFINEMENT MODULE WITH TREE-ENERGY LOSS [21].  $pr\_lmi$  MEANS MUTUAL INFORMATION APPROXIMATION FROM [5].  $pr\_mi$  IS THE RESULT BASED ON  $pr\_rd$  WITH THE MUTUAL INFORMATION REGULARIZATION TERM.

Method	NJU2K [3]				SSB [118]				DES [30]				NLPR [4]				LFSD [119]				SIP [120]			
	$S_\alpha \uparrow$	$F_\beta \uparrow$	$E_\xi \uparrow$	$\mathcal{M} \downarrow$	$S_\alpha \uparrow$	$F_\beta \uparrow$	$E_\xi \uparrow$	$\mathcal{M} \downarrow$	$S_\alpha \uparrow$	$F_\beta \uparrow$	$E_\xi \uparrow$	$\mathcal{M} \downarrow$	$S_\alpha \uparrow$	$F_\beta \uparrow$	$E_\xi \uparrow$	$\mathcal{M} \downarrow$	$S_\alpha \uparrow$	$F_\beta \uparrow$	$E_\xi \uparrow$	$\mathcal{M} \downarrow$	$S_\alpha \uparrow$	$F_\beta \uparrow$	$E_\xi \uparrow$	$\mathcal{M} \downarrow$
$r\_d$	.852	.827	.906	.063	.845	.803	.900	.066	.900	.858	.949	.033	.865	.810	.922	.042	.802	.779	.847	.106	.839	.815	.902	.067
$pr\_rd$	.891	.879	.929	.046	.887	.862	.926	.047	.917	.901	.953	.023	.909	.881	.945	.029	.834	.819	.865	.088	.860	.835	.906	.060
$pr\_lmi$	.883	.863	.921	.049	.884	.852	.921	.050	.912	.888	.948	.026	.906	.873	.942	.030	.828	.808	.856	.088	.858	.832	.899	.063
$pr\_mi$	.891	.880	.927	.046	.892	.870	.929	.044	.918	.901	.952	.024	.906	.882	.942	.028	.829	.816	.864	.086	.866	.846	.911	.057

TABLE V

PERFORMANCE OF PREDICTION REFINEMENT TECHNIQUES, WHERE  $D\_s$  IS OBTAINED BY DIRECTLY APPLYING FIRST STAGE OUTPUT AS PSEUDO LABEL, AND  $D\_crf$  IS ACHIEVED VIA APPLYING DENSECRF [29] AS POST-PROCESSING TECHNIQUE.

Method	NJU2K [3]				SSB [118]				DES [30]				NLPR [4]				LFSD [119]				SIP [120]			
	$S_\alpha \uparrow$	$F_\beta \uparrow$	$E_\xi \uparrow$	$\mathcal{M} \downarrow$	$S_\alpha \uparrow$	$F_\beta \uparrow$	$E_\xi \uparrow$	$\mathcal{M} \downarrow$	$S_\alpha \uparrow$	$F_\beta \uparrow$	$E_\xi \uparrow$	$\mathcal{M} \downarrow$	$S_\alpha \uparrow$	$F_\beta \uparrow$	$E_\xi \uparrow$	$\mathcal{M} \downarrow$	$S_\alpha \uparrow$	$F_\beta \uparrow$	$E_\xi \uparrow$	$\mathcal{M} \downarrow$	$S_\alpha \uparrow$	$F_\beta \uparrow$	$E_\xi \uparrow$	$\mathcal{M} \downarrow$
$pr\_mi$	.891	.880	.927	.046	.892	.870	.929	.044	.918	.901	.952	.024	.906	.882	.942	.028	.829	.816	.864	.086	.866	.846	.911	.057
$D\_s$	.894	.885	.930	.044	.888	.868	.929	.045	.908	.894	.942	.025	.907	.883	.947	.027	.837	.826	.873	.085	.875	.863	.919	.051
$D\_crf$	.885	.886	.929	.045	.887	.880	.930	.040	.896	.892	.938	.024	.897	.886	.939	.027	.823	.824	.863	.083	.864	.855	.915	.054
Ours	.890	.880	.929	.046	.891	.873	.934	.042	.928	.921	.965	.019	.914	.895	.953	.025	.849	.844	.889	.072	.876	.863	.924	.049

fuse RGB and depth structural and localization information on the prediction, we introduce the graph based progressive refinement module with tree-energy loss [21] based on  $r\_d(r\_d(RV))$  in Table III). The performance of the model with tree-energy loss is  $pr\_rd$  in Table IV. We observe significant performance improvement compared with  $r\_d$ , verifying its effectiveness.

**Mutual information regularization analysis:** Built upon  $pr\_rd$ , we further encourage disentangled representation across modalities with mutual information minimization and show its performance as  $pr\_mi$  in Table IV. To explain the superiority of our mutual information upper bound compared with an existing solution in [5], we replace our  $I_{mi}$  term from Eq. (7) with mutual information approximation from [5]. The performance is shown as  $pr\_lmi$  in Table IV. The improved performance of  $pr\_mi$  compared with both  $pr\_rd$  and  $pr\_lmi$  explains the contribution of the mutual information regularization term.

**Prediction refinement strategies analysis:** Following the conventional prediction refinement pipeline, we refine the first stage prediction via both pseudo labeling as second stage training and denseCRF [29] as post-processing technique, and show the performance in Table V as  $D_s$  and  $D_{crf}$  respectively. Similar to the proposed MVAE refinement method,  $D_s$  uses trained model prediction on the training dataset in the first stage as a pseudo-label. The network of  $D_s$  uses the same network structure as the first training network. Same as our MVAE refine model, using structure-aware loss function [132] to emphasize the structural details of the predictions. Moreover, we post-process the predictions of  $pr\_mi$  with denseCRF [29] and compare it with our proposed refinement method, where parameters of denseCRF are set in line with [133]. The results are shown as  $D_{crf}$ . Table V shows that the proposed solution works better than the existing techniques, achieving boost performance.

## V. CONCLUSION

We introduced a weakly-supervised RGB-D salient object detection model with scribble supervision. Five main strategies are introduced in our framework to achieve accurate predictions. Firstly, we find that the RGB and depth modalities respond differently to the same backbone, and we propose to extract features of the two modalities using asymmetric encoders. Secondly, we design a simple cross-modal fusion module, achieving significant performance improvement compared with the baseline RGB based model and early fusion RGB-D model. Thirdly, we incorporate minimum spanning tree based tree-energy loss into our framework to achieve training time prediction refinement, encouraging unlabeled pixels in model updating. Fourthly, we present mutual information minimization as a regularizer to extensively model the contribution of RGB image and depth data for effective multimodal fusion. Lastly, our stochastic multimodal VAE based prediction refinement strategy is proven effective and robust for our weakly-supervised learning task.

**Limitations:** According to Table IV, mutual information minimization fails to consistently improve model performance. We analyze predictions before and after using  $\mathcal{L}_{mi}$  and find that noisy depth signal can be enhanced with the proposed regularizer. Our next step is then to further incorporate a noise robust regularizer to prevent the model from being influenced by the noisy modality. Comparing “ $D_{crf}$ ” and “Our” of Table V, the performance of our proposed MVAE refinement is slightly lower than CRF refinement for some metrics in the NJU2K and SSB datasets. It can be found that learning-based optimization is a double-edged sword in that MVAE can balance the contribution of RGB and depth to prediction while can also be misled by both of them. In addition, due to extra parameters involved, MVAE [18]–[20] will be further investigated to extensively explore its contribution as a prediction refinement technique.

## REFERENCES

- [1] L. Wang, H. Lu, Y. Wang, M. Feng, D. Wang, B. Yin, and X. Ruan, "Learning to detect salient objects with image-level supervision," in *IEEE Conference on Computer Vision and Pattern Recognition (CVPR)*, 2017, pp. 136–145.
- [2] M.-M. Cheng, N. J. Mitra, X. Huang, P. H. S. Torr, and S.-M. Hu, "Global contrast based salient region detection," *IEEE Transactions on Pattern Analysis and Machine Intelligence (TPAMI)*, vol. 37, no. 3, pp. 569–582, 2015.
- [3] R. Ju, Y. Liu, T. Ren, L. Ge, and G. Wu, "Depth-aware salient object detection using anisotropic center-surround difference," *Signal Processing: Image Communication*, vol. 38, pp. 115 – 126, 2015.
- [4] H. Peng, B. Li, W. Xiong, W. Hu, and R. Ji, "Rgb-d salient object detection: a benchmark and algorithms," in *European Conference on Computer Vision (ECCV)*, 2014, pp. 92–109.
- [5] J. Zhang, D.-P. Fan, Y. Dai, X. Yu, Y. Zhong, N. Barnes, and L. Shao, "Rgb-d saliency detection via cascaded mutual information minimization," in *International Conference on Computer Vision (ICCV)*, 2021.
- [6] Y. Piao, J. Wang, M. Zhang, and H. Lu, "Mfnet: Multi-filter directive network for weakly supervised salient object detection," in *IEEE Conference on Computer Vision and Pattern Recognition (CVPR)*, 2021, pp. 4136–4145.
- [7] G. Li, Y. Xie, and L. Lin, "Weakly supervised salient object detection using image labels," in *AAAI Conference on Artificial Intelligence (AAAI)*, 2018.
- [8] K.-J. Hsu, Y.-Y. Lin, and Y.-Y. Chuang, "Weakly supervised salient object detection by learning a classifier-driven map generator," *IEEE Transactions on Image Processing (TIP)*, vol. 28, no. 11, pp. 5435–5449, 2019.
- [9] Y. Piao, J. Wang, M. Zhang, Z. Ma, and H. Lu, "To be critical: Self-calibrated weakly supervised learning for salient object detection," *arXiv preprint arXiv:2109.01770*, 2021.
- [10] Y. Piao, W. Wu, M. Zhang, Y. Jiang, and H. Lu, "Noise-sensitive adversarial learning for weakly supervised salient object," *IEEE Transactions on Multimedia (TMM)*, 2022.
- [11] R. Yasarla, R. Weng, W. Choi, V. Patel, and A. Sadeghian, "3sd: Self-supervised saliency detection with no labels," *arXiv preprint arXiv:2203.04478*, 2022.
- [12] S. Yu, B. Zhang, J. Xiao, and E. G. Lim, "Structure-consistent weakly supervised salient object detection with local saliency coherence," in *AAAI Conference on Artificial Intelligence (AAAI)*, 2021, pp. 3234–3242.
- [13] J. Zhang, X. Yu, A. Li, P. Song, B. Liu, and Y. Dai, "Weakly-supervised salient object detection via scribble annotations," in *IEEE Conference on Computer Vision and Pattern Recognition (CVPR)*, 2020, pp. 12 546–12 555.
- [14] Y. Xu, X. Yu, J. Zhang, L. Zhu, and D. Wang, "Weakly supervised rgb-d salient object detection with prediction consistency training and active scribble boosting," *IEEE Transactions on Image Processing (TIP)*, vol. 31, pp. 2148–2161, 2022.
- [15] Y. Liu, P. Wang, Y. Cao, Z. Liang, and R. W. Lau, "Weakly-supervised salient object detection with saliency bounding boxes," *IEEE Transactions on Image Processing (TIP)*, vol. 30, pp. 4423–4435, 2021.
- [16] P. Cheng, W. Hao, S. Dai, J. Liu, Z. Gan, and L. Carin, "Club: A contrastive log-ratio upper bound of mutual information," in *International Conference on Machine Learning (ICML)*, 2020, pp. 1779–1788.
- [17] A. Rangarajan and A. L. Yuille, "Mime: Mutual information minimization and entropy maximization for bayesian belief propagation," in *Advances in Neural Information Processing Systems (NeurIPS)*, 2001.
- [18] D. P. Kingma and M. Welling, "Auto-encoding variational bayes," in *International Conference on Learning Representations (ICLR)*, 2013.
- [19] K. Sohn, H. Lee, and X. Yan, "Learning structured output representation using deep conditional generative models," in *Advances in Neural Information Processing Systems (NeurIPS)*, 2015, pp. 3483–3491.
- [20] M. Wu and N. D. Goodman, "Multimodal generative models for scalable weakly-supervised learning," in *Advances in Neural Information Processing Systems (NeurIPS)*, 2018, pp. 5580–5590.
- [21] Z. Liang, T. Wang, X. Zhang, J. Sun, and J. Shen, "Tree energy loss: Towards sparsely annotated semantic segmentation," in *IEEE Conference on Computer Vision and Pattern Recognition (CVPR)*, 2022, pp. 16907–16916.
- [22] R. T. Chen, X. Li, R. B. Grosse, and D. K. Duvenaud, "Isolating sources of disentanglement in variational autoencoders," in *Advances in Neural Information Processing Systems (NeurIPS)*, 2018.
- [23] X. Zhao, Y. Pang, L. Zhang, H. Lu, and X. Ruan, "Self-supervised pretraining for rgb-d salient object detection," in *AAAI Conference on Artificial Intelligence (AAAI)*, 2022.
- [24] W. Ji, J. Li, S. Yu, M. Zhang, Y. Piao, S. Yao, Q. Bi, K. Ma, Y. Zheng, H. Lu *et al.*, "Calibrated rgb-d salient object detection," in *IEEE Conference on Computer Vision and Pattern Recognition (CVPR)*, 2021, pp. 9471–9481.
- [25] P. Sun, W. Zhang, H. Wang, S. Li, and X. Li, "Deep rgb-d saliency detection with depth-sensitive attention and automatic multi-modal fusion," in *IEEE Conference on Computer Vision and Pattern Recognition (CVPR)*, 2021, pp. 1407–1417.
- [26] M. Hu, X. Zhang, and L. Zhao, "Multi-scale residual interaction for rgb-d salient object detection," in *Asian Conference on Computer Vision (ACCV)*, 2022, pp. 2494–2509.
- [27] Y. Wang and Y. Zhang, "Three-stage bidirectional interaction network for efficient rgb-d salient object detection," in *Asian Conference on Computer Vision (ACCV)*, 2022, pp. 3672–3689.
- [28] Q. Chen, Z. Liu, Y. Zhang, K. Fu, Q. Zhao, and H. Du, "Rgb-d salient object detection via 3d convolutional neural networks," in *AAAI Conference on Artificial Intelligence (AAAI)*, 2021, pp. 1063–1071.
- [29] P. Krähenbühl and V. Koltun, "Efficient inference in fully connected crfs with gaussian edge potentials," in *Advances in Neural Information Processing Systems (NeurIPS)*, J. Shawe-Taylor, R. S. Zemel, P. L. Bartlett, F. Pereira, and K. Q. Weinberger, Eds., 2011, pp. 109–117.
- [30] Y. Cheng, H. Fu, X. Wei, J. Xiao, and X. Cao, "Depth enhanced saliency detection method," in *Proceedings of international conference on internet multimedia computing and service*, 2014, pp. 23–27.
- [31] X. Zhao, L. Zhang, Y. Pang, H. Lu, and L. Zhang, "A single stream network for robust and real-time rgb-d salient object detection," in *European Conference on Computer Vision (ECCV)*, 2020.
- [32] Y. Piao, Z. Rong, M. Zhang, W. Ren, and H. Lu, "A2dele: Adaptive and attentive depth distiller for efficient rgb-d salient object detection," in *IEEE Conference on Computer Vision and Pattern Recognition (CVPR)*, 2020.
- [33] K. Fu, D.-P. Fan, G.-P. Ji, and Q. Zhao, "Jl-dcf: Joint learning and densely-cooperative fusion framework for rgb-d salient object detection," in *IEEE Conference on Computer Vision and Pattern Recognition (CVPR)*, 2020, pp. 3052–3062.
- [34] Y. Piao, W. Ji, J. Li, M. Zhang, and H. Lu, "Depth-induced multi-scale recurrent attention network for saliency detection," in *IEEE International Conference on Computer Vision (ICCV)*, 2019.
- [35] H. Chen and Y. Li, "Progressively complementarity-aware fusion network for RGB-D salient object detection," in *IEEE Conference on Computer Vision and Pattern Recognition (CVPR)*, 2018, pp. 3051–3060.
- [36] G. Li, Z. Liu, L. Ye, Y. Wang, and H. Ling, "Cross-modal weighting network for rgb-d salient object detection," in *European Conference on Computer Vision (ECCV)*, 2020.
- [37] Z. Wu, S. Gobichettipalayam, B. Tamadazte, G. Allibert, D. P. Paudel, and C. Démonceaux, "Robust RGB-D fusion for saliency detection," in *International Conference on 3D Vision (3DV)*, 2022.
- [38] Y.-H. Wu, Y. Liu, J. Xu, J.-W. Bian, Y.-C. Gu, and M.-M. Cheng, "Mobilesal: Extremely efficient rgb-d salient object detection," *IEEE Transactions on Pattern Analysis and Machine Intelligence (TPAMI)*, 2021.
- [39] Y. Mao, J. Zhang, Z. Wan, Y. Dai, A. Li, Y. Lv, X. Tian, D.-P. Fan, and N. Barnes, "Generative transformer for accurate and reliable salient object detection," *arXiv e-prints*, pp. arXiv:2104, 2021.
- [40] W. Zhang, Y. Jiang, K. Fu, and Q. Zhao, "Bts-net: Bi-directional transfer-and-selection network for rgb-d salient object detection," in *ICME*, 2021.
- [41] Y. Yang, Q. Qin, Y. Luo, Y. Liu, Q. Zhang, and J. Han, "Bi-directional progressive guidance network for rgb-d salient object detection," *IEEE Transactions on Circuits and Systems for Video Technology (TCSVT)*, vol. 32, no. 8, pp. 5346–5360, 2022.
- [42] W. Gao, G. Liao, S. Ma, G. Li, Y. Liang, and W. Lin, "Unified information fusion network for multi-modal rgb-d and rgb-t salient object detection," *IEEE Transactions on Circuits and Systems for Video Technology (TCSVT)*, vol. 32, no. 4, pp. 2091–2106, 2021.
- [43] Z. Liu, Y. Tan, Q. He, and Y. Xiao, "Swinnet: Swin transformer drives edge-aware rgb-d and rgb-t salient object detection," *IEEE Transactions on Circuits and Systems for Video Technology (TCSVT)*, vol. 32, no. 7, pp. 4486–4497, 2021.
- [44] X. Jin, K. Yi, and J. Xu, "Moadnet: Mobile asymmetric dual-stream networks for real-time and lightweight rgb-d salient object detection," *IEEE Transactions on Circuits and Systems for Video Technology (TCSVT)*, vol. 32, no. 11, pp. 7632–7645, 2022.

- [45] G. Chen, F. Shao, X. Chai, H. Chen, Q. Jiang, X. Meng, and Y.-S. Ho, "Modality-induced transfer-fusion network for rgb-d and rgb-t salient object detection," *IEEE Transactions on Circuits and Systems for Video Technology (TCSVT)*, vol. 33, no. 4, pp. 1787–1801, 2023.
- [46] T. Zhou, H. Fu, G. Chen, Y. Zhou, D.-P. Fan, and L. Shao, "Specificity-preserving rgb-d saliency detection," in *IEEE Conference on Computer Vision and Pattern Recognition (CVPR)*, 2021, pp. 4681–4691.
- [47] M. Zhang, W. Ren, Y. Piao, Z. Rong, and H. Lu, "Select, supplement and focus for rgb-d saliency detection," in *IEEE Conference on Computer Vision and Pattern Recognition (CVPR)*, 2020, pp. 3472–3481.
- [48] N. Wang and X. Gong, "Adaptive fusion for rgb-d salient object detection," *IEEE Access*, vol. 7, pp. 55 277–55 284, 2019.
- [49] Y.-f. Zhang, J. Zheng, W. Jia, W. Huang, L. Li, N. Liu, F. Li, and X. He, "Deep rgb-d saliency detection without depth," *IEEE Transactions on Multimedia (TMM)*, vol. 24, pp. 755–767, 2021.
- [50] J. Zhang, D.-P. Fan, Y. Dai, S. Anwar, F. Sadat Saleh, T. Zhang, and N. Barnes, "Uc-net: Uncertainty inspired rgb-d saliency detection via conditional variational autoencoders," in *IEEE Conference on Computer Vision and Pattern Recognition (CVPR)*, 2020.
- [51] X. Tian, K. Xu, X. Yang, B. Yin, and R. W. H. Lau, "Learning to detect instance-level salient objects using complementary image labels," *International Journal of Computer Vision (IJCV)*, 2022.
- [52] X. Zheng, X. Tan, J. Zhou, L. Ma, and R. W. H. Lau, "Weakly-supervised saliency detection via salient object subitizing," *IEEE Transactions on Circuits and Systems for Video Technology (TCSVT)*, vol. 31, no. 11, pp. 4370–4380, 2021.
- [53] Y. Wang, W. Zhang, L. Wang, T. Liu, and H. Lu, "Multi-source uncertainty mining for deep unsupervised saliency detection," in *Proceedings of the IEEE/CVF Conference on Computer Vision and Pattern Recognition (CVPR)*, June 2022, pp. 11 727–11 736.
- [54] J. Zhang, T. Zhang, Y. Dai, M. Harandi, and R. Hartley, "Deep unsupervised saliency detection: A multiple noisy labeling perspective," in *IEEE Conference on Computer Vision and Pattern Recognition (CVPR)*, 2018, pp. 9029–9038.
- [55] D. Zhang, J. Han, and Y. Zhang, "Supervision by fusion: Towards unsupervised learning of deep salient object detector," in *2017 IEEE International Conference on Computer Vision (ICCV)*, 2017, pp. 4068–4076.
- [56] J. Zhang, J. Xie, and N. Barnes, "Learning noise-aware encoder-decoder from noisy labels by alternating back-propagation for saliency detection," *European Conference on Computer Vision (ECCV)*, 2020.
- [57] T. Nguyen, M. Dax, C. K. Mummadi, N. Ngo, T. H. P. Nguyen, Z. Lou, and T. Brox, "Deepusps: Deep robust unsupervised saliency prediction via self-supervision," in *Advances in Neural Information Processing Systems (NeurIPS)*, 2019.
- [58] J. Zhang, Y. Dai, T. Zhang, M. Harandi, N. Barnes, and R. Hartley, "Learning saliency from single noisy labelling: A robust model fitting perspective," *IEEE Transactions on Pattern Analysis and Machine Intelligence (TPAMI)*, vol. 43, no. 8, pp. 2866–2873, 2020.
- [59] W. Ji, J. Li, Q. Bi, chuan guo, J. Liu, and L. Cheng, "Promoting saliency from depth: Deep unsupervised RGB-d saliency detection," in *International Conference on Learning Representations (ICLR)*, 2022.
- [60] M. Feng, K. Liu, L. Zhang, H. Yu, Y. Wang, and A. Mian, "Learning from pixel-level noisy label: A new perspective for light field saliency detection," in *IEEE Conference on Computer Vision and Pattern Recognition (CVPR)*, 2022, pp. 1756–1766.
- [61] W. Zhao, J. Zhang, L. Li, N. Barnes, N. Liu, and J. Han, "Weakly supervised video salient object detection," in *IEEE Conference on Computer Vision and Pattern Recognition (CVPR)*, 2021, pp. 16 826–16 835.
- [62] S. Gao, X. Haozhe, W. Zhang, Y. Wang, Q. Guo, and W. Zhang, "Weakly supervised video salient object detection via point supervision," in *ACM International Conference on Multimedia (MM)*, 2022, pp. 3656–3665.
- [63] B. Zhou, A. Khosla, A. Lapedriza, A. Oliva, and A. Torralba, "Learning deep features for discriminative localization," in *IEEE Conference on Computer Vision and Pattern Recognition (CVPR)*, 2016, pp. 2921–2929.
- [64] J. Shi and J. Malik, "Normalized cuts and image segmentation," *IEEE Transactions on Pattern Analysis and Machine Intelligence (TPAMI)*, vol. 22, no. 8, pp. 888–905, 2000.
- [65] R. Urquhart, "Graph theoretical clustering based on limited neighbourhood sets," *Pattern Recognition (PR)*, vol. 15, no. 3, pp. 173–187, 1982.
- [66] Z. Wu and R. Leahy, "An optimal graph theoretic approach to data clustering: Theory and its application to image segmentation," *IEEE Transactions on Pattern Analysis and Machine Intelligence (TPAMI)*, vol. 15, no. 11, pp. 1101–1113, 1993.
- [67] C. T. Zahn, "Graph-theoretical methods for detecting and describing gestalt clusters," *IEEE Transactions on computers*, vol. 100, no. 1, pp. 68–86, 1971.
- [68] C. Yang, L. Zhang, H. Lu, X. Ruan, and M.-H. Yang, "Saliency detection via graph-based manifold ranking," in *IEEE Conference on Computer Vision and Pattern Recognition (CVPR)*, 2013, pp. 3166–3173.
- [69] Ç. Aytekin, A. Iosifidis, S. Kiranyaz, and M. Gabbouj, "Learning graph affinities for spectral graph-based salient object detection," *Pattern Recognition*, vol. 64, pp. 159–167, 2017.
- [70] S. Lu, V. Mahadevan, and N. Vasconcelos, "Learning optimal seeds for diffusion-based salient object detection," in *IEEE Conference on Computer Vision and Pattern Recognition (CVPR)*, 2014, pp. 2790–2797.
- [71] V. Gopalakrishnan, Y. Hu, and D. Rajan, "Random walks on graphs for salient object detection in images," *IEEE Transactions on Image Processing (TIP)*, vol. 19, no. 12, pp. 3232–3242, 2010.
- [72] W.-C. Tu, S. He, Q. Yang, and S.-Y. Chien, "Real-time salient object detection with a minimum spanning tree," in *2016 IEEE Conference on Computer Vision and Pattern Recognition (CVPR)*, 2016, pp. 2334–2342.
- [73] T. Zhang, Y. Zhou, S. Huo, and C. Hou, "Label propagation based saliency detection via graph design," in *2017 IEEE International Conference on Image Processing (ICIP)*, 2017, pp. 460–464.
- [74] Y. Liu, J. Han, Q. Zhang, and L. Wang, "Salient object detection via two-stage graphs," *IEEE Transactions on Circuits and Systems for Video Technology (TCSVT)*, vol. 29, no. 4, pp. 1023–1037, 2019.
- [75] F. Wang and G. Peng, "Graph-based saliency detection using a learning joint affinity matrix," *Neurocomputing*, vol. 458, pp. 33–46, 2021.
- [76] Y. Xiao, B. Jiang, A. Zheng, A. Zhou, A. Hussain, and J. Tang, "Saliency detection via multi-view graph based saliency optimization," *Neurocomputing*, vol. 351, pp. 156–166, 2019.
- [77] Y. Zhou, T. Zhang, S. Huo, C. Hou, and S.-Y. Kung, "Adaptive irregular graph construction-based salient object detection," *IEEE Transactions on Circuits and Systems for Video Technology (TCSVT)*, vol. 30, no. 6, pp. 1569–1582, 2020.
- [78] K.-J. Hsu, C.-C. Tsai, Y.-Y. Lin, X. Qian, and Y.-Y. Chuang, "Unsupervised cnn-based co-saliency detection with graphical optimization," in *Proceedings of the European Conference on Computer Vision (ECCV)*, September 2018.
- [79] Z. Li, C. Lang, J. Feng, Y. Li, T. Wang, and S. Feng, "Co-saliency detection with graph matching," *ACM Transactions on Intelligent Systems and Technology (TIST)*, vol. 10, no. 3, pp. 1–22, 2019.
- [80] K. Zhang, T. Li, S. Shen, B. Liu, J. Chen, and Q. Liu, "Adaptive graph convolutional network with attention graph clustering for co-saliency detection," in *Proceedings of the IEEE/CVF Conference on Computer Vision and Pattern Recognition (CVPR)*, June 2020.
- [81] R. Hu, Z. Deng, and X. Zhu, "Multi-scale graph fusion for co-saliency detection," in *Proceedings of the Thirty-Fifth Conference on Association for the Advancement of Artificial Intelligence (AAAI)*, 2021, pp. 7789–7796.
- [82] T. Li, K. Zhang, S. Shen, B. Liu, Q. Liu, and Z. Li, "Image co-saliency detection and instance co-segmentation using attention graph clustering based graph convolutional network," *IEEE Transactions on Multimedia (TMM)*, vol. 24, pp. 492–505, 2021.
- [83] M. Xu, P. Fu, B. Liu, and J. Li, "Multi-stream attention-aware graph convolution network for video salient object detection," *IEEE Transactions on Image Processing (TIP)*, vol. 30, pp. 4183–4197, 2021.
- [84] J. B. Kinney and G. S. Atwal, "Equitability, mutual information, and the maximal information coefficient," *Proceedings of the National Academy of Sciences*, vol. 111, no. 9, pp. 3354–3359, 2014.
- [85] B. Poole, S. Ozair, A. Van Den Oord, A. Alemi, and G. Tucker, "On variational bounds of mutual information," in *International Conference on Machine Learning (ICML)*, 2019, pp. 5171–5180.
- [86] D. Barber and F. V. Agakov, "The im algorithm: A variational approach to information maximization," in *Advances in Neural Information Processing Systems (NeurIPS)*, 2003, pp. 201–208.
- [87] E. H. Sanchez, M. Serrurier, and M. Ortner, "Learning disentangled representations via mutual information estimation," in *European Conference on Computer Vision (ECCV)*, 2020, pp. 205–221.
- [88] P. Colombo, C. Clavel, and P. Piantanida, "A novel estimator of mutual information for learning to disentangle textual representations," *arXiv preprint arXiv:2105.02685*, 2021.

- [89] D. Xin, T. Komatsu, S. Takamichi, and H. Saruwatari, "Disentangled speaker and language representations using mutual information minimization and domain adaptation for cross-lingual tts," in *IEEE International Conference on Acoustics, Speech and Signal Processing (ICASSP)*. IEEE, 2021, pp. 6608–6612.
- [90] X. Ma, X. Kong, S. Zhang, and E. Hovy, "Decoupling global and local representations via invertible generative flows," *arXiv preprint arXiv:2004.11820*, 2020.
- [91] G. Gao, H. Huang, C. Fu, Z. Li, and R. He, "Information bottleneck disentanglement for identity swapping," in *IEEE Conference on Computer Vision and Pattern Recognition (CVPR)*, 2021, pp. 3404–3413.
- [92] S. Soleymani, A. Dabouei, F. Taherkhani, J. Dawson, and N. M. Nasrabadi, "Mutual information maximization on disentangled representations for differential morph detection," in *IEEE Winter Conference on Applications of Computer Vision (WACV)*, 2021, pp. 1731–1741.
- [93] Y. Xiao and W. Y. Wang, "Disentangled representation learning with wasserstein total correlation," *arXiv preprint arXiv:1912.12818*, 2019.
- [94] M. Lee and V. Pavlovic, "Private-shared disentangled multimodal vae for learning of latent representations," in *IEEE Conference on Computer Vision and Pattern Recognition (CVPR) Workshop*, 2021, pp. 1692–1700.
- [95] I. Daunhawer, T. M. Sutter, R. Marcinkevičs, and J. E. Vogt, "Self-supervised disentanglement of modality-specific and shared factors improves multimodal generative models," in *DAGM German Conference on Pattern Recognition*. Springer, 2020, pp. 459–473.
- [96] D. H. Wolpert and D. R. Wolf, "Estimating functions of probability distributions from a finite set of samples," *Physical Review E*, vol. 52, no. 6, p. 6841, 1995.
- [97] M. Hutter, "Distribution of mutual information," in *Advances in Neural Information Processing Systems (NeurIPS)*, 2001.
- [98] E. Archer, I. M. Park, and J. W. Pillow, "Bayesian and quasi-bayesian estimators for mutual information from discrete data," *Entropy*, vol. 15, no. 5, pp. 1738–1755, 2013.
- [99] G. Shin, W. Xie, and S. Albanie, "All you need are a few pixels: semantic segmentation with pixelpick," in *IEEE International Conference on Computer Vision (ICCV)*, 2021, pp. 1687–1697.
- [100] J. Li, J. Fan, and Z. Zhang, "Towards noiseless object contours for weakly supervised semantic segmentation," in *IEEE Conference on Computer Vision and Pattern Recognition (CVPR)*, 2022, pp. 16856–16865.
- [101] J. Lee, E. Kim, and S. Yoon, "Anti-adversarially manipulated attributions for weakly and semi-supervised semantic segmentation," in *IEEE Conference on Computer Vision and Pattern Recognition (CVPR)*, 2021, pp. 4071–4080.
- [102] Y. Li, Z. Kuang, L. Liu, Y. Chen, and W. Zhang, "Pseudo-mask matters in weakly-supervised semantic segmentation," in *IEEE International Conference on Computer Vision (ICCV)*, 2021, pp. 6964–6973.
- [103] J. Lee, J. Choi, J. Mok, and S. Yoon, "Reducing information bottleneck for weakly supervised semantic segmentation," *Advances in Neural Information Processing Systems (NeurIPS)*, vol. 34, pp. 27 408–27 421, 2021.
- [104] J. Ahn, S. Cho, and S. Kwak, "Weakly supervised learning of instance segmentation with inter-pixel relations," in *IEEE Conference on Computer Vision and Pattern Recognition (CVPR)*, 2019, pp. 2209–2218.
- [105] J. Ahn and S. Kwak, "Learning pixel-level semantic affinity with image-level supervision for weakly supervised semantic segmentation," in *IEEE Conference on Computer Vision and Pattern Recognition (CVPR)*, 2018, pp. 4981–4990.
- [106] R. Ranftl, K. Lasinger, D. Hafner, K. Schindler, and V. Koltun, "Towards robust monocular depth estimation: Mixing datasets for zero-shot cross-dataset transfer," *IEEE Transactions on Pattern Analysis and Machine Intelligence (TPAMI)*, vol. 44, no. 3, 2022.
- [107] K. Simonyan and A. Zisserman, "Very deep convolutional networks for large-scale image recognition," in *International Conference on Learning Representations (ICLR)*, 2014.
- [108] K. He, X. Zhang, S. Ren, and J. Sun, "Deep residual learning for image recognition," in *IEEE Conference on Computer Vision and Pattern Recognition (CVPR)*, 2016, pp. 770–778.
- [109] M. Tang, A. Djelouah, F. Perazzi, Y. Boykov, and C. Schroers, "Normalized cut loss for weakly-supervised cnn segmentation," in *IEEE Conference on Computer Vision and Pattern Recognition (CVPR)*, 2018, pp. 1818–1827.
- [110] G. E. Hinton, "Training products of experts by minimizing contrastive divergence," *Neural Comput.*, vol. 14, no. 8, p. 1771–1800, 2002.
- [111] Y. Cao and D. J. Fleet, "Generalized product of experts for automatic and principled fusion of gaussian process predictions," *arXiv preprint arXiv:1410.7827*, 2014.
- [112] A. Neelakantan, L. Vilnis, Q. V. Le, I. Sutskever, L. Kaiser, K. Kurach, and J. Martens, "Adding gradient noise improves learning for very deep networks," *arXiv preprint arXiv:1511.06807*, 2015.
- [113] I. Higgins, L. Matthey, A. Pal, C. Burgess, X. Glorot, M. Botvinick, S. Mohamed, and A. Lerchner, "beta-vae: Learning basic visual concepts with a constrained variational framework," in *International Conference on Learning Representations (ICLR)*, 2017.
- [114] W. Wang, E. Xie, X. Li, D.-P. Fan, K. Song, D. Liang, T. Lu, P. Luo, and L. Shao, "Pyramid vision transformer: A versatile backbone for dense prediction without convolutions," in *IEEE International Conference on Computer Vision (ICCV)*, 2021, pp. 568–578.
- [115] Z. Liu, Y. Lin, Y. Cao, H. Hu, Y. Wei, Z. Zhang, S. Lin, and B. Guo, "Swin transformer: Hierarchical vision transformer using shifted windows," in *IEEE International Conference on Computer Vision (ICCV)*, 2021.
- [116] M. Sandler, A. Howard, M. Zhu, A. Zhmoginov, and L.-C. Chen, "Mobilenetv2: Inverted residuals and linear bottlenecks," in *IEEE Conference on Computer Vision and Pattern Recognition (CVPR)*, 2018, pp. 4510–4520.
- [117] L. Yuan, Y. Chen, T. Wang, W. Yu, Y. Shi, Z.-H. Jiang, F. E. Tay, J. Feng, and S. Yan, "Tokens-to-token vit: Training vision transformers from scratch on imagenet," in *IEEE International Conference on Computer Vision (ICCV)*, 2021, pp. 558–567.
- [118] Y. Niu, Y. Geng, X. Li, and F. Liu, "Leveraging stereopsis for saliency analysis," in *IEEE Conference on Computer Vision and Pattern Recognition (CVPR)*, 2012, pp. 454–461.
- [119] N. Li, J. Ye, Y. Ji, H. Ling, and J. Yu, "Saliency detection on light field," in *IEEE Conference on Computer Vision and Pattern Recognition (CVPR)*, 2014, pp. 2806–2813.
- [120] D.-P. Fan, Z. Lin, Z. Zhang, M. Zhu, and M.-M. Cheng, "Rethinking RGB-D salient object detection: Models, datasets, and large-scale benchmarks," *IEEE Transactions on Neural Networks and Learning Systems (TNNLS)*, 2020.
- [121] N. Liu, N. Zhang, K. Wan, L. Shao, and J. Han, "Visual saliency transformer," in *IEEE International Conference on Computer Vision (ICCV)*, 2021, pp. 4722–4732.
- [122] J. Zhang, J. Xie, N. Barnes, and P. Li, "Learning generative vision transformer with energy-based latent space for saliency prediction," in *Advances in Neural Information Processing Systems (NeurIPS)*. Curran Associates, Inc., 2021, pp. 15 448–15 463.
- [123] M. Zhang, S. Yao, B. Hu, Y. Piao, and W. Ji, "C2dfnet: Criss-cross dynamic filter network for rgb-d salient object detection," *IEEE Transactions on Multimedia (TMM)*, 2022.
- [124] R. Cong, Q. Lin, C. Zhang, C. Li, X. Cao, Q. Huang, and Y. Zhao, "Cinnet: Cross-modality interaction and refinement for rgb-d salient object detection," *IEEE Transactions on Image Processing (TIP)*, vol. 31, pp. 6800–6815, 2022.
- [125] J. Li, W. Ji, Q. Bi, C. Yan, M. Zhang, Y. Piao, H. Lu *et al.*, "Joint semantic mining for weakly supervised rgb-d salient object detection," *Advances in Neural Information Processing Systems (NeurIPS)*, vol. 34, pp. 11 945–11 959, 2021.
- [126] T. Yang, Y. Wang, L. Zhang, J. Qi, and H. Lu, "Depth-inspired label mining for unsupervised rgb-d salient object detection," in *ACM International Conference on Multimedia (MM)*, 2022, pp. 5669–5677.
- [127] S. W. Jun Wei and Q. Huang, "F3net: Fusion, feedback and focus for salient object detection," in *AAAI Conference on Artificial Intelligence (AAAI)*, 2020.
- [128] D.-P. Fan, G.-P. Ji, X. Qin, and M.-M. Cheng, "Cognitive vision inspired object segmentation metric and loss function," *SCIENTIA SINICA Informationis*, vol. 6, p. 6, 2021.
- [129] D.-P. Fan, M.-M. Cheng, Y. Liu, T. Li, and A. Borji, "Structure-measure: A new way to evaluate foreground maps," in *IEEE International Conference on Computer Vision (ICCV)*, 2017, pp. 4548–4557.
- [130] J. Deng, W. Dong, R. Socher, L.-J. Li, K. Li, and L. Fei-Fei, "Imagenet: A large-scale hierarchical image database," in *IEEE Conference on Computer Vision and Pattern Recognition (CVPR)*, 2009, pp. 248–255.
- [131] Z. Wu, L. Su, and Q. Huang, "Cascaded partial decoder for fast and accurate salient object detection," in *IEEE Conference on Computer Vision and Pattern Recognition (CVPR)*, 2019.
- [132] J. Wei, S. Wang, and Q. Huang, "F3net: Fusion, feedback and focus for salient object detection," in *AAAI Conference on Artificial Intelligence (AAAI)*, 2020, pp. 12 321–12 328.
- [133] L. Melas-Kyriazi, C. Rupprecht, I. Laina, and A. Vedaldi, "Deep spectral methods: A surprisingly strong baseline for unsupervised semantic segmentation and localization," in *IEEE Conference on Computer Vision and Pattern Recognition (CVPR)*, 2022, pp. 8364–8375.



**Aixuan Li** currently is a PhD student majoring in signal and information processing in the School of Electronics and Information, Northwestern Polytechnical University. Her main research direction is salient object detection and camouflaged object detection. She received the M.E. degree of signal and information processing from Northwestern Polytechnical University, 2022.



**Yuxin Mao** is currently a PhD student with School of Electronics and Information, Northwestern Polytechnical University, Xi'an, China. He received his Bachelor of Engineering degree from Southwest Jiaotong University in 2020. He won the best Paper Award Nominee at ICIUS 2019.



**Jing Zhang** is currently a Lecturer with School of Computing, the Australian National University (Canberra, Australia). Her main research interests include saliency detection, weakly supervised learning, generative models. She won the Best Student Paper Prize at DICTA 2017, the Best Deep/Machine Learning Paper Prize at APSIPA ASC 2017 and the Best Paper Award Nominee at IEEE CVPR 2020.



**Yuchao Dai** is currently a Professor with School of Electronics and Information at the Northwestern Polytechnical University (NPU). He received the B.E. degree, M.E degree and Ph.D. degree all in signal and information processing from NPU, Xi'an, China, in 2005, 2008 and 2012, respectively. He was an ARC DECRA Fellow with the Research School of Engineering at the Australian National University, Canberra, Australia. His research interests include 3D vision, multi-view geometry, low-level vision, deep learning, and optimization. He won the Best

Paper Award in IEEE CVPR 2012, Best Paper Nominee in IEEE CVPR 2020, the DSTO Best Fundamental Contribution to Image Processing Paper Prize at DICTA 2014, the Best Algorithm Prize in NRSFM Challenge at CVPR 2017, the Best Student Paper Prize at DICTA 2017 and the Best Deep/Machine Learning Paper Prize at APSIPA ASC 2017. He served/serves as Area Chair at CVPR, ICCV, NeurIPS, ACM MM, etc. He serves as the Publicity Chair at ACCV 2022 and the Distinguished Lecturer of APSIPA.